Analysis of the electron downstream boundary conditions in a 2D hybrid code for Hall thrusters

IEPC-2022-338

Presented at the 37th International Electric Propulsion Conference
Massachusetts Institute of Technology, Cambridge, MA, USA
June 19-23, 2022

Adrian Domínguez-Vázquez [1], Jiewei Zhou [2], Alejandro Sevillano-González [3], Pablo Fajardo [4] and Eduardo Ahedo [5]
Equipo de Propulsión Espacial y Plasmas (EP2), Universidad Carlos III de Madrid, 28911 Leganés, Spain

This work presents a new model providing boundary conditions for electron fluid models of electromagnetic plasma thrusters to be imposed at the quasineutral boundary of the finite plume domain. Contrary to the null local current condition, the new model locally decouples ion and electron currents at the plume boundary, obtains a final potential in the plume assuring a globally current-free plasma plume, and provides expressions for the electron particle and energy fluxes at the quasineutral plume boundary. Numerical simulations of a virtual 5kW-class Hall effect thruster yield more consistent and robust results against the plume truncation for the longitudinal electron and electric current maps in the near plume, than for the case of a locally current-free plume. Current and power balances show similar discharge performances with the plume size and the electron boundary condition downstream.

I. Introduction

Electromagnetic plasma thruster discharge simulation codes are essential for facilitating the design and optimization of thruster prototypes, as they offer a deeper insight into the operation physical mechanisms and provide valuable estimations of the thruster performance and operational lifetime, thus reducing development time and costs.

For both mature technologies such as the Hall effect thruster (HET) [1, 2] and novel electrodeless plasma thruster (EPT) technologies, including the electron cyclotron resonance thruster (ECRT) [3, 4] and the helicon plasma thruster (HPT) [5–8], hybrid particle-in-cell (PIC)/fluid [9, 10] and multi-fluid [11, 12] simulation models are attractive approaches describing the main physical phenomenon of interest while avoiding prohibitive simulation times. For a precise characterization of the discharge performance, the simulation domain must include the near plume region extending downstream the thruster chamber. However, simulating very large plumes is computationally expensive. Therefore, setting appropriate boundary conditions at the downstream plume boundary of the finite simulation domain is of central importance. These must reproduce faithfully the plasma expansion to infinity, where a final electric potential is reached in the globally current-free plasma plume.

The simple null local current condition is commonly imposed for the current-free plasma beam downstream [9, 11]. Previous works on a mini-HPT have shown that this condition is not robust against the truncation of the simulated plume domain, yielding significantly different longitudinal electric current maps in the plume if the plume size is not large enough [13]. Moreover, this boundary condition gives no information about the final potential in the plume nor the electron energy flux through the plume boundary. Recent analyses on a virtual EPT have revealed that the electron temperature solution in a truncated plume is largely affected by the uncertain electron heat flux at the plume boundary [14]. Furthermore, multi-fluid simulations have shown that the electron cooling in a magnetic nozzle is very sensitive to the type of boundary condition imposed at the outflow boundary in terms of the electron heat flux [15].

[1]Assistant professor, Bioengineering and Aerospace Engineering Department, adrian.dominguez@uc3m.es.
[2]Assistant professor, Bioengineering and Aerospace Engineering Department, jiewei.zhou@uc3m.es.
[3]MSc student, Bioengineering and Aerospace Engineering Department, alesevil@pa.uc3m.es.
[4]Full professor, Bioengineering and Aerospace Engineering Department, pablo.fajardo@uc3m.es.
[5]Full professor, Bioengineering and Aerospace Engineering Department, eduardo.ahedo@uc3m.es.

Previous kinetic studies for both magnetized [16] and unmagnetized [17, 18] plume expansions, have found that relevant features of the dynamics of the expansion are comparable to those of a Debye sheath. Based on the analogy, a global downstream matching layer (GDML) model for the off-simulation region, including electron dynamics, is presented in this work. The GDML is defined as a thin boundary layer relating relevant electron magnitudes at the quasineutral downstream plume boundary of the finite simulation domain and the infinity. The model permits to estimate a plume final potential at infinity assuring a globally current-free plasma plume, while locally decouples ion and electron currents at the plume boundary of the finite domain, and provides expressions for the electron particle and energy fluxes at the quasineutral plume boundary. The performance of the GDML is evaluated and compared against the local null current condition for a virtual 5kW-class HET through numerical simulations performed with HYPHEN, a 2D axisymmetric hybrid PIC/fluid code with application to several electromagnetic thrusters, including HET [19–22] and EPT [13, 14, 23]. The simulation results will show that the GDML yields a more consistent solution for the longitudinal electron currents in the plume, better capturing the behaviour of the still significantly magnetized electron population in the near plume region of a HET. Moreover, simulations for different plume sizes will prove the GDML to be more robust against the plume truncation, limiting the influence of the plume boundary on the longitudinal electric current solution and the ion beam neutralization downstream, and thus increasing the reliability of the simulation results obtained for smaller, less computationally demanding plume domains.

The rest of the paper is organized as follows. Section II outlines the main characteristics of the HYPHEN code, focusing on the electron fluid model and the development and implementation of the GDML model. Section III gathers the simulation results and their discussion as follows. Section III.A describes the simulation settings and define the simulation scenarios analyzed in this work. Section III.B presents the assessment of the electron downstream boundary conditions for a given plume domain size. Section III.C addresses the ion current and plasma power balances of the plasma discharge, along with relevant discharge performances. Section III.D analyzes plume extension effects. Section IV summarizes the conclusions.

II. The HYPHEN simulation code

HYPHEN is a two-dimensional, axisymmetric, hybrid, PIC/fluid, OpenMP-parallelized, multi-thruster simulation code. The main characteristics of the simulator have been detailed in Refs. [13, 14, 19–21, 23–26], and are briefly outlined next for the HET version of HYPHEN, used in this work.

Figure 1 shows a sketch of the HYPHEN code structure and simulation loop. The three main modules of the simulation tool are: the ion module (I-module), which follows a Lagrangian approach for the simulation of the dynamics of the heavy species (i.e. ions and neutrals); the electron module (E-module), which solves a fluid model for the magnetized electron population and applies quasineutrality; and a sheath module (S-module) that provides the proper matching between the thruster walls and the quasineutral plasma by solving the Debye sheaths adjacent to the thruster walls, which are thus treated as discontinuity surfaces. The three modules above are coupled within a time-marching sequential loop.

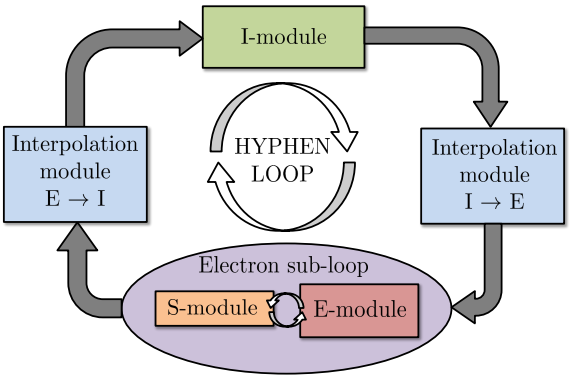

Fig. 1 HYPHEN main simulation loop and modules.

The simulation domain geometry is sketched in Fig. 2(a). The plasma domain to be simulated with HYPHEN corresponds to the cylindrical axisymmetric half meridian plane, including the annular thruster chamber and the near plume region. The geometrical parameters L_c and H_c correspond to the thruster chamber length and width, respectively,

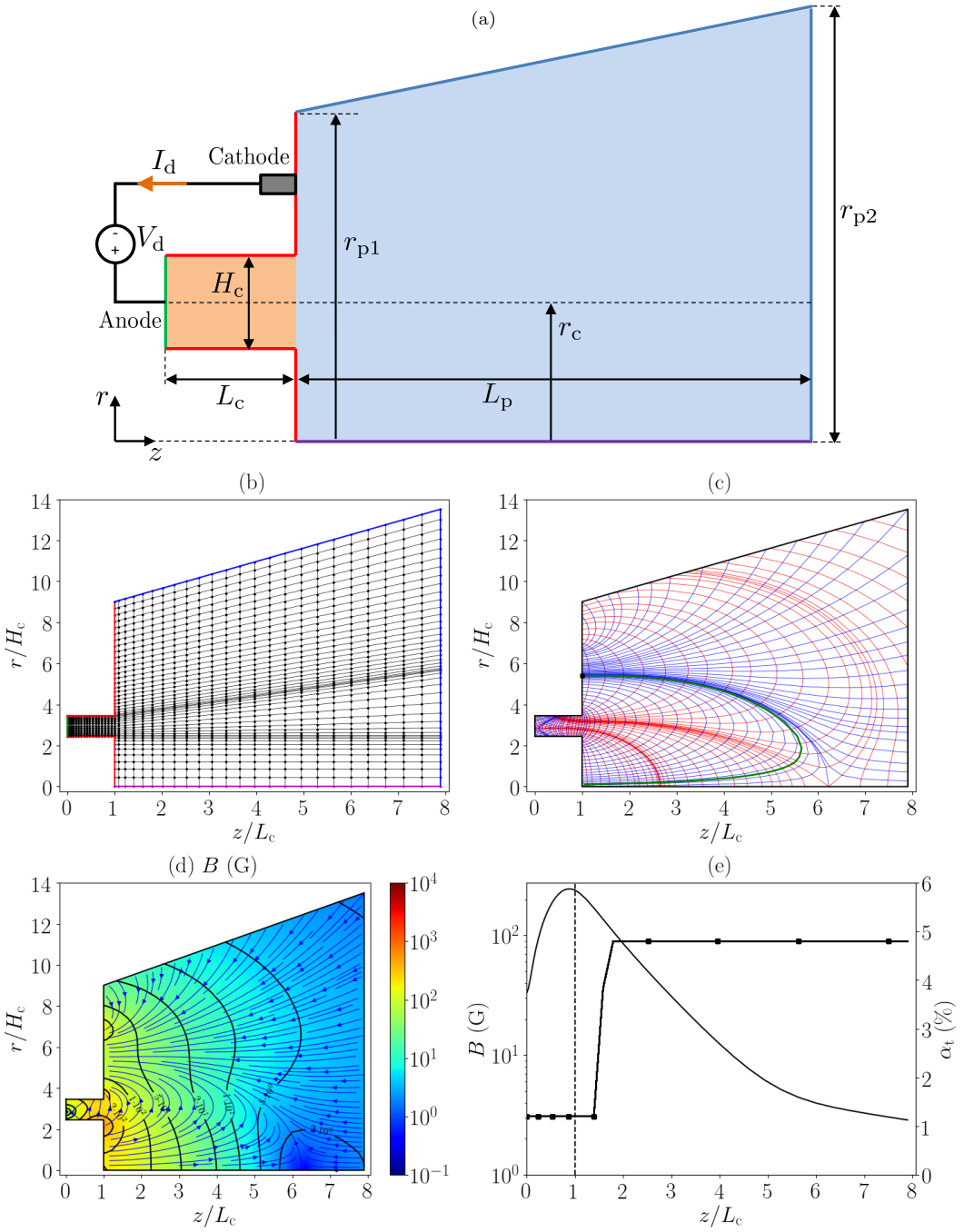

Fig. 2 (a) Sketch of the simulation domain. Dimensions listed in Table 1. (b) Structured mesh used by the I-module. The red, green, blue and magenta lines indicate the thruster dielectric walls, the anode wall, the downstream plume boundary P, and the symmetry axis, respectively. (c) The MFAM used by the E-module. Blue and red lines are B-parallel and B-perpendicular lines, respectively, defining the cells. The black square marker indicates the position of the external cathode at the boundary wall. The green line identifies the cathode magnetic line. (d) 2D map of the magnetic field magnitude. (e) 1D axial profiles along the thruster channel midline of the B magnitude (solid black line and left y-axis) and the "step-out" type α_t function used for all simulation cases presented in this work (solid black line with square markers and right y-axis).

while L_p, r_p1 and r_p2 indicate the axial and radial extent of the near plume region. The position of the external cathode exit plane, is also indicated in Fig. 2(a).

Figure 2(b) shows the structured mesh of the simulation domain used by the I-module, which is defined on the cylindrical reference frame $\{\mathbf{1}_\mathrm{z}, \mathbf{1}_\mathrm{r}, \mathbf{1}_\theta\}$, with coordinates (z, r, θ). On the other hand, the E-module uses an unstructured magnetic field aligned mesh (MFAM) [27] to limit the numerical diffusion arising from the strong anisotropic transport of magnetized electrons, which is depicted in Fig. 2(c). An interpolation module enables the communication between both the I and E-modules. The MFAM is obtained from the externally applied, axisymmetric magnetic field $\boldsymbol{B}$, whose 2D contour map and axial profile along the thruster channel midline are shown in Figs. 2(d) and 2(e), respectively; and is defined on a magnetically aligned frame $\{\mathbf{1}_\perp, \mathbf{1}_\parallel, \mathbf{1}_\theta\}$, with $\mathbf{1}_\parallel = \boldsymbol{B}/B$ and $\mathbf{1}_\perp = 1_\parallel \times 1_\theta$, and coordinates $(\lambda, \sigma, \theta)$. The MFAM orthogonal magnetic coordinates $\lambda(z, r)$ and $\sigma(z, r)$ are obtained from solving the solenoidal and irrotational conditions for the axisymmetric applied magnetic field, $\nabla \cdot \boldsymbol{B} = 0$ and $\nabla \times \boldsymbol{B} = 0$. Blue and red lines defining MFAM cells in Fig. 2(c) correspond to λ and σ isolines, thus aligned with B-parallel and B-perpendicular directions, respectively.

Let us define Z_s, n_s, $\boldsymbol{u}_\mathrm{s}$, and $\boldsymbol{j}_\mathrm{s} = eZ_\mathrm{s}n_\mathrm{s}\boldsymbol{u}_\mathrm{s}$ as the charge number, particle density, macroscopic velocity, and current density of the plasma species s (e.g., electrons e, neutrals n, singly-charged ions i1, and doubly-charged ions i2); $\boldsymbol{E} = -\nabla\phi$ as the electric field, with ϕ the electric potential; and T_e as the electron temperature. Every complete HYPHEN simulation step, the I-module takes as inputs $\boldsymbol{B}$, $\boldsymbol{E}$, ϕ and T_e, and performs (i) the propagation of ion and neutral macroparticles one simulation timestep Δt forward, according to the electromagnetic fields acting on them; (ii) the injection of new macroparticles into the domain and the removal of exiting ones across the domain boundaries; (iii) the macroparticles interaction with the material walls, such as ion recombination or neutral reflection; (iv) the collisional processes between the heavy species macroparticles and with the electrons (i.e., generation of new ion macroparticles from ionization collisions and generation of slow ion and fast neutral macroparticles from charge-exchange (CEX) collisions); and (v) the computation, by means of a particle-to-mesh weighting process, of the macroscopic properties characterizing each heavy species. More details on this module can be found in Refs. [19, 24, 25].

Then, the E-module takes as inputs the heavy species magnitudes (mainly particle densities and fluxes for the different heavy species, e.g., neutrals n, singly-charged ions i1 and doubly-charged ions i2) and solves a quasineutral, drift-diffusion fluid model for the magnetized electron population, obtaining ϕ, T_e, and the electron current density and heat flux vectors $\boldsymbol{j}_\mathrm{e}$ and $\boldsymbol{q}_\mathrm{e}$, respectively. The model equations are [28–30]

$$n_\mathrm{e} = \sum_{\mathrm{s}\neq\mathrm{e,n}} Z_\mathrm{s} n_\mathrm{s}, \tag{1}$$

$$\nabla \cdot \boldsymbol{j}_\mathrm{e} = -\nabla \cdot \boldsymbol{j}_\mathrm{i}, \tag{2}$$

$$0 = -\nabla(n_\mathrm{e}T_\mathrm{e}) + en_\mathrm{e}\nabla\phi + \boldsymbol{j}_\mathrm{e} \times \boldsymbol{B} + \boldsymbol{F}_\mathrm{res} + \boldsymbol{F}_\mathrm{t}, \tag{3}$$

$$\frac{\partial}{\partial t}\left(\frac{3}{2}n_\mathrm{e}T_\mathrm{e}\right) + \nabla \cdot \left(\frac{5}{2}n_\mathrm{e}T_\mathrm{e}\boldsymbol{u}_\mathrm{e} + \boldsymbol{q}_\mathrm{e}\right) = -\boldsymbol{j}_\mathrm{e} \cdot \nabla\phi - P'''_\mathrm{inel}. \tag{4}$$

$$\boldsymbol{q}_\mathrm{e} = -\bar{\bar{K}}_\mathrm{e} \cdot \nabla T_\mathrm{e} \tag{5}$$

Plasma quasineutrality corresponds to Eq. (1), while Eq. (2) states the conservation of electric current density $\boldsymbol{j} = \boldsymbol{j}_\mathrm{e} + \boldsymbol{j}_\mathrm{i}$, with $\boldsymbol{j}_i = \sum_{\mathrm{s}\neq\mathrm{e,n}} \boldsymbol{j}_\mathrm{s}$ the total ion current. The right hand sides of Eqs. (1) and (2) are inputs from the I-module. Due to plasma quasineutrality and the absence of volumetric sources of net current, Eq. (2) for the current conservation is much more convenient numerically than the electron continuity equation, $\partial n_\mathrm{e}/\partial t + \nabla \cdot n_\mathrm{e}\boldsymbol{u}_\mathrm{e} = S_\mathrm{e}$, where S_e is the source term of electrons. In the hybrid formulation followed here, S_e is computed by the I-module through the ionization events for both singly and doubly charged ions, as explained in previous works [24, 28, 31, 32]. Collision data comes from the BIAGI database [33] for single-ion generation, and the Drawin model [34] for double-ion generation.

Equation (3) is the electron momentum equation in the inertialess limit, assuming an isotropic electron pressure tensor, and including the resistive force $\boldsymbol{F}_\mathrm{res}$ and the turbulent (or anomalous) force $\boldsymbol{F}_\mathrm{t}$. The former is

$$\boldsymbol{F}_\mathrm{res} = (m_\mathrm{e}\nu_\mathrm{e}/e)(\boldsymbol{j}_\mathrm{e} + \boldsymbol{j}_\mathrm{c}), \tag{6}$$

with m_e the electron elementary mass, $\nu_\mathrm{e} = \sum_{\mathrm{s}\neq\mathrm{e}} \nu_\mathrm{es}$ the total momentum transfer frequency due to collisions with all heavy species, ν_es the individual contributions for each heavy species s, and $\boldsymbol{j}_\mathrm{c} = en_\mathrm{e}\sum_{\mathrm{s}\neq\mathrm{e}}(\nu_\mathrm{es}/\nu_\mathrm{e})\boldsymbol{u}_\mathrm{s}$ an equivalent heavy species collisional current density [19]. A phenomenological model is considered for the azimuth-averaged, wave-based electron anomalous transport turbulent force $\boldsymbol{F}_\mathrm{t}$ [9, 28, 35, 36]

$$\boldsymbol{F}_\mathrm{t} = -m_\mathrm{e}\nu_\mathrm{t}n_\mathrm{e}u_{\theta\mathrm{e}}\mathbf{1}_\theta, \qquad \nu_\mathrm{t} = \alpha_\mathrm{t}\omega_\mathrm{ce}, \tag{7}$$

with ν_t a turbulent collision frequency, $\omega_{ce} = eB/m_e$ the electron gyrofrequency, and $\alpha_t(z,r)$ a phenomenological function representing the local turbulence level [9, 28]. Turbulent-based contributions to the axial and radial momentum equations are negligible compared to the rest of forces there.

Neglecting electron inertia in Eq. (3) is the main model assumption here, which is justified as long as the electron kinetic energy is much lower than their thermal energy, i.e., $m_e u_e^2 \ll T_e$, a condition well satisfied in HET discharges except in localized regions and certain operation points. This assumption greatly simplifies the numerical integration, since it permits to reduce the Eq. (3) to a generalized Ohm's law for the electron current density $\boldsymbol{j}_e$, which includes an electric conductivity tensor $\bar{\bar{\sigma}}_e$, and whose components in the magnetic frame are

$$j_{\parallel e} = \sigma_{\parallel e}\left[\frac{1}{en_e}\frac{\partial(n_e T_e)}{\partial \mathbf{1}_\parallel} - \frac{\partial\phi}{\partial \mathbf{1}_\parallel}\right] - j_{\parallel c}, \tag{8}$$

$$j_{\perp e} = \sigma_{\perp e}\left[\frac{1}{en_e}\frac{\partial(n_e T_e)}{\partial \mathbf{1}_\perp} - \frac{\partial\phi}{\partial \mathbf{1}_\perp}\right] - \frac{j_{\perp c} - \chi_t j_{\theta c}}{1+\chi\chi_t}, \tag{9}$$

$$j_{\theta e} = \chi_t j_{\perp e} - \frac{\chi_t}{\chi} j_{\theta c}, \tag{10}$$

where

$$\sigma_{\parallel e} = \frac{e^2 n_e}{m_e \nu_e}, \qquad \sigma_{\perp e} = \frac{e^2 n_e}{m_e(\nu_e+\nu_t)} = \frac{\sigma_{\parallel e}}{1+\chi\chi_t}, \tag{11}$$

are the scalar B-parallel and B-perpendicular electric conductivities, respectively, $\chi = \omega_{ce}/\nu_e$ is the classical Hall parameter and $\chi_t = \chi/(1+\alpha_t\chi)$ is the reduced Hall parameter when including ν_t. Therefore, the effective Hall parameter is $\sqrt{\chi\chi_t}$ and scales as $\propto \alpha_t^{-1/2}$ if turbulent transport dominates.

Equation (4) corresponds to the inertialess electron energy equation for an isotropic pressure tensor. The second term in the left side is the electron energy flux

$$\boldsymbol{P}_e'' = -\frac{5}{2}T_e \boldsymbol{j}_e/e + \boldsymbol{q}_e, \tag{12}$$

gathering the enthalpy and heat fluxes. The right side includes the work of the electric field and the power losses from inelastic collisions (e.g., excitation and ionization). The Fourier's law for the heat flux in Eq. (5) corresponds to the drift-diffusion limit of the evolution equation for $\boldsymbol{q}_e$ [29]. The components of $\boldsymbol{q}_e$ on the magnetic reference frame read

$$q_{\parallel e} = -K_{\parallel e}\frac{\partial T_e}{\partial \mathbf{1}_\parallel}, \tag{13}$$

$$q_{\perp e} = -K_{\perp e}\frac{\partial T_e}{\partial \mathbf{1}_\perp}, \tag{14}$$

$$q_{\theta e} = \chi_t q_{\perp e}, \tag{15}$$

the thermal conductivity tensor being $\bar{\bar{K}}_e = 5T_e\bar{\bar{\sigma}}_e/(2e^2)$.

A detailed description of the numerical treatment of Eqs. (2)-(5) solving for ϕ, T_e, $\boldsymbol{j}_e$ and $\boldsymbol{q}_e$ in the unstructured, irregular MFAM can be found in Refs. [13, 14, 23, 27], and it is briefly outlined here. The MFAM is composed of inner and boundary cells, as shown in Fig. 2(c). Inner cells are those enclosed by B-parallel (blue) and B-perpendicular (red) lines. Boundary cells, however, contain at least one boundary face aligned with a domain boundary, which is not a magnetic line generally. Centroids (or computational points) of both cell and faces correspond to the magnetic center or the geometric center, when the former is not available (e.g., at boundary cells). Equations (2) and (4) are discretized in the MFAM through a finite volume method (FVM); and a gradient reconstruction method (GRM) developed for the unstructured MFAM is applied to Ohm's and Fourier's vector laws in Eqs. (3) and (5), respectively. For each variable ϕ and T_e, this generates one algebraic equation per MFAM cell. Boundary conditions (discussed later) specifying $j_{ne} = \mathbf{1}_n \cdot \boldsymbol{j}_e$ and $P''_{ne} = \mathbf{1}_n \cdot \boldsymbol{P}''_e$ are imposed at each MFAM boundary face, with $\mathbf{1}_n$ being the *outward* unit normal vector. The reference for the potential ($\phi = 0$) is set at the cathode boundary faces, so that the current-driving anode wall is set at a known discharge voltage $\phi = V_d$. The resulting FVM/GRM spatial discretization yields matrix equations for both ϕ and T_e at the centroids of the cells and of the boundary faces of the MFAM. A direct solver for sparse linear systems is used for the parallelized computation of the solution [37, 38].

The boundary conditions imposed in terms of j_{ne} and P''_{ne} depend on the type of boundary, as follows. At dielectric and metallic walls, such as the thruster chamber lateral and anode walls, respectively, the simulation domain is bounded by the sheath edge of the quasineutral plasma, represented by the MFAM boundary faces. The solution for the (infinitely) thin Debye sheaths, computed by the S-module, is described in the Appendix. The appropriate values for j_{ne} and P''_{ne} at each quasineutral MFAM boundary face are provided in Eqs. (29) and (33), respectively, in the form of non-linear relations versus the potential jump across the sheath, ϕ_{WQ}. At a dielectric wall, the zero-collected electric current condition imposes $j_{ne} = -j_{ni}$. Then, Eqs. (29) and (33) solve for ϕ_{WQ} and P''_{ne}, respectively. At the metallic, current-driving anode wall, at known discharge potential V_d, the determination of j_{ne} and P''_{ne}, at each anode face of the MFAM, requires to solve first for ϕ_{WQ} in an iterative way: at each anode face, Eq. (29) is combined with the Ohm's law in Eq. (3) for j_{ne} yielding a non-linear implicit equation for $\phi_Q = V_d + \phi_{WQ}$, which is linearized, incorporated to the matrix system for ϕ, and solved iteratively if required.

At the (quasineutral) axis, symmetry conditions imply $j_{ne} = 0$ and $q_{ne} = 0$, so that $P''_{ne} = 0$. Since the I-module yields $\partial n_e/\partial r = 0$, this implies $\partial(n_e T_e)/\partial r = 0$ and $\partial\phi/\partial r = 0$. At the cathode boundary faces, the discharge current I_d divided by the cathode area defines the electron current density $j_{ne}(> 0)$. The electron energy flux at each cathode face, is set as $P''_{ne} = -2T_c j_{ne}/e$, with $2T_c$ the average emission energy per electron. At the (quasineutral) downstream plume boundary P, the new GDML model providing the appropriate boundary conditions is presented in Sec. II.A.

The time discretization of the electron equations follows a semi-implicit scheme [14, 23, 26], with a sub-timestep $\Delta t_e = \Delta t/N_e$ and $N_e = O(1)$. This scheme allows to keep a linear system for T_e while reducing the value of N_e required for convergence.

A. Boundary conditions at the downstream plume boundary

The local null current condition at P

$$j_{neP} = -j_{niP}, \tag{16}$$

gives no information about the value of final electric potential far downstream in the plume ϕ_∞ nor the electron energy flux leaving the finite domain. When Eq. (16) is imposed in HYPHEN, the electron energy flux at a given MFAM boundary face at P is set to

$$P''_{neP} = -cT_{eP} j_{neP}/e, \tag{17}$$

with $c > 0$ a given constant parameter. Matching this energy flux with that given in Eq. (12) yields the electron heat flux at P

$$q_{neP} = -c_q T_{eP} j_{neP}/e, \tag{18}$$

where $c_q = c - 5/2$. Values of $c = 5/2$, $9/2$ and $13/2$, corresponding to $c_q = 0$, 2 and 4, respectively, were simulated in Ref. [14] for a virtual EPT, revealing a significant impact of c on the electron temperature solution for truncated plume domains, $c = 9/2$ yielding a better agreement among the results for two different plume domain sizes. Here, we set $c = 9/2$ when the local null current condition is applied at P.

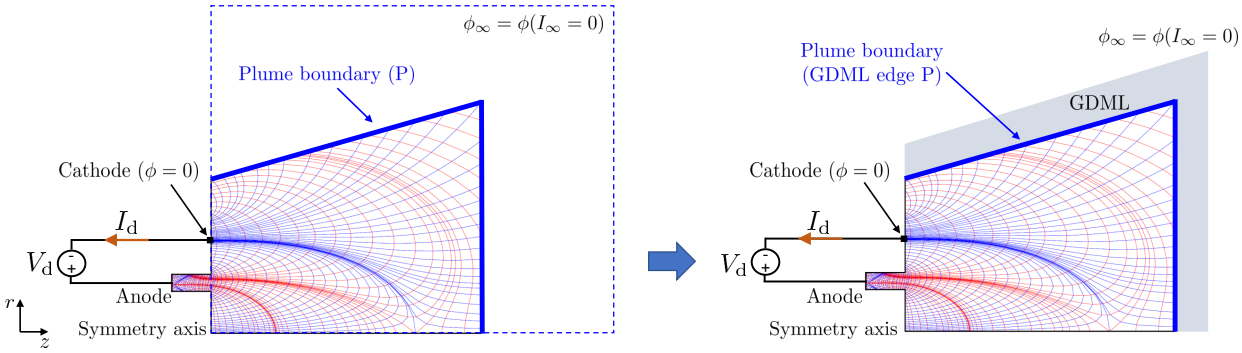

Fig. 3 Sketch of the GDML model for the boundary condition at the downstream plume boundary P of the finite simulation domain.

A new GDML model for the off-simulation region, summarizing the electron dynamics in the infinite plume expansion, is proposed here. The GDML is defined as a thin boundary layer providing the jump conditions for relevant

electron magnitudes between P and the infinity, as sketched in Fig. 3. A first version of the GDML (partially similar to a classical Debye sheath) permits to obtain ϕ_∞ (i.e., infinity-to-cathode bias) by imposing a global zero current condition at P

$$I_\infty = I_{e\infty} + I_{i\infty} = \int_P (j_{ne} + j_{ni}) dS = \int_P (j_{ne}(\phi_{\infty P}) + j_{ni}) dS = 0, \tag{19}$$

where the surface integral is performed over P, $I_{e\infty}$ and $I_{i\infty}$ being the total electron and ion currents collected at P, respectively. In Eq. (19), at each MFAM boundary face belonging to P, the collected ion current density j_{ni} is provided by the I-module. Similarly to the case of a metallic boundary, outlined in Sec. II, the determination of j_{ne} at a given MFAM boundary face belonging to P requires to obtain first the local P-to-infinity potential fall $\phi_{\infty P} = \phi_P - \phi_\infty$, with ϕ_P being the local potential at the quasineutral boundary face (with respect to cathode). For each boundary face of P, and taking δ_s, $\delta_r = 0$ and $\phi_{WQ} \equiv \phi_{\infty P}$, the following iterative procedure is applied. Equation (29) is combined with the Ohm's law in Eq. (3) for j_{ne} yielding a non-linear implicit equation for $\phi_P = \phi_\infty + \phi_{\infty P}$. This equation is linearized, incorporated to the matrix system for ϕ and solved iteratively if required. Equation (19), solving for ϕ_∞, closes the matrix system for ϕ.

From Eqs. (32) and (33), the electron energy fluxes at infinity and at P are

$$P''_{ne\infty} = -2T_{eP} j_{neP}/e, \tag{20}$$

$$P''_{neP} = P''_{ne\infty} - j_{neP}\phi_{\infty P}. \tag{21}$$

Matching P''_{neP} to that from the quasineutral domain, $\mathbf{1}_n \cdot \boldsymbol{P}''_e$, with $\boldsymbol{P}''_e$ from Eq. (12), the electron heat flux at P is

$$q_{neP} = P''_{neP} + \frac{5}{2} T_{eP} j_{neP}/e. \tag{22}$$

III. Simulation results and discussion

A. Simulation settings

The simulation results presented in this work correspond to the VHET-US, a 5kW-class virtual thruster designed by the EP2 research group at Universidad Carlos III de Madrid (UC3M). Figure 2(a) sketches the thruster chamber geometry, with dimensions listed in Table 1. Four different plume domains, with increasing length L_p and maximum radius r_{p2} are considered, and referred to as P1, P2, P3 and P4, for which the near plume region extends axially up to 3.5, 6.9, 10.3 and 13.8 channel lengths, respectively (see dimensions in Table 1). The VHET-US features an unshielded magnetic topology (US) generated through the commercial software FEMM [39]. For the P2 case, Figs. 2(d) and 2(e) show, respectively, the 2D map of the applied $\boldsymbol{B}$ magnitude and streamlines, and the axial profile along the thruster channel midline of B. The MFAM shown in Fig. 2(c) is obtained from the applied magnetic field. The magnetic field intensity peak value and its location along the thruster channel midline are listed in Table 1, along with the average B value at the downstream plume boundary P for cases P1 to P4. The structured mesh used by the I-module for the case P2 is shown in Fig. 2(b). In the plume region, the cells approximately follow the ion beam expansion to limit PIC-related statistical noise induced by particle depletion. The different simulation domain boundary types are indicated as follows: the red, green, blue and magenta lines correspond to the thruster dielectric walls, the anode wall, the downstream plume boundary P, and the symmetry axis, respectively. The main characteristics of the simulation domain meshes for cases P1 to P4 are listed in Table 1.

For all cases considered in this work, a single thruster operating point with xenon as propellant is simulated, defined in terms of the anode-to-cathode discharge voltage V_d, and the xenon mass flows injected through the anode and the cathode, $\dot{m}_A$ and $\dot{m}_C$, respectively (refer to Table 1). The mass flow $\dot{m}_A$ is injected from a Maxwellian reservoir through the whole annular anode featuring a flat profile with a sonic axial velocity based on its own temperature (see Table 1). The cathode mass flow $\dot{m}_C$ is injected through the cathode boundary with the same injection properties. As described in Sec. II, the reference for the potential ($\phi = 0$) is set at the cathode boundary, so that the anode wall is set at $\phi = V_d$. An electron current equal to the discharge current I_d collected at the anode is injected through the cathode boundary into the simulation domain. The average cathode emission energy per electron is set to $2T_c = 4.5$ eV [40].

Wall recombination of ions contributes to the neutral density. Singly and doubly charged ions are generated volumetrically by electron-neutral collisions. Double ionization collisions include the reactions $Xe + e \rightarrow Xe^{++} + 3e$,

Simulation parameter	Units	Value
Thruster chamber length, L_c	mm	29
Thruster chamber width, H_c	mm	22.20
Thruster chamber mid radius, r_c	mm	65.60
Plume length, L_p (P1, P2, P3, P4)	mm	100, 200, 300, 400
Plume min. radius, r_{p1}	mm	200
Plume max. radius, r_{p2} (P1, P2, P3, P4)	mm	250, 300, 350, 400
Cathode location, z, r	mm	29, 120
I-module mesh smallest grid size	mm	1
I-module mesh number of cells (P1, P2, P3, P4)	-	969, 1284, 1509, 1734
I-module mesh number of nodes (P1, P2, P3, P4)	-	1049, 1371, 1601, 2831
MFAM number of cells (P1, P2, P3, P4)	-	1948, 2397, 3506, 4081
MFAM number of faces (P1, P2, P3, P4)	-	4025, 4933, 7186, 8353
MFAM average cells skewness (P1, P2, P3, P4)	-	0.0706, 0.0645, 0.0549, 0.0531
Ion-moving timestep, Δt	ns	15
Total number of simulation steps	-	60000
B peak along the channel midline	G	245.06
Axial location of the B peak along the channel midline	mm	25
Average B at P (P1, P2, P3, P4)	G	10.53, 5.81, 4.67, 3.93
Discharge voltage, V_d	V	300
Anode Xe mass flow rate, $\dot{m}_A$	mg/s	17.59
Cathode Xe mass flow rate, $\dot{m}_C$	mg/s	1.32
Injected Xe velocity	ms^{-1}	300 (sonic)
Injected Xe temperature	K	850

Table 1 Main simulation parameters and mesh characteristics.

Simulation case	Description
P1L	Plume size P1, local zero current at P
P2L	Plume size P2, local zero current at P
P3L	Plume size P3, local zero current at P
P4L	Plume size P4, local zero current at P
P1G	Plume size P1, GDML at P
P2G	Plume size P2, GDML at P
P3G	Plume size P3, GDML at P
P4G	Plume size P4, GDML at P

Table 2 Simulation cases definition.

and $Xe^+ + e \rightarrow Xe^{++} + 2e$. Neutrals from ion recombination at walls are re-emitted diffusely considering complete ion energy accommodation at the wall. Thus, the neutral emission energy is only given by the wall temperature, which is set to 850K [41]. Neutrals undergo a quasi-specular reflection at the walls according to Schamberg model [42, 43] with complete energy accommodation; Refs. [19, 25] provide further details on the interaction of heavy species macroparticles with walls.

The following resonant-symmetric CEX reactions, with no momentum exchange, are considered through a

Direct Simulation Monte Carlo (DSMC) algorithm [19, 32]: $Xe^{+}(fast) + Xe(slow) \rightarrow Xe^{+}(slow) + Xe(fast)$, and $Xe^{++}(fast) + Xe(slow) \rightarrow Xe^{++}(slow) + Xe(fast)$. The CEX cross section for both CEX reactions is provided for xenon gas by the Miller model [44].

The simulations monitor independently the populations of both fast and slow (i.e., product of a CEX reaction) neutrals, singly-charged and doubly-charged ions. Each species population is controlled, setting a target number of 200 macroparticles per cell with a ±10% of tolerance [19].

The simulation or ion-moving timestep in Table 1 is set so that a typical fast doubly-charged ion takes at least two timesteps to cross the smallest PIC cell. The simulations are started by injecting neutrals through the anode and cathode and considering a minimum background plasma density to trigger the discharge [25]. Every simulation features a total of 60000 timesteps (equivalent to 900 μs of simulation time) so that I_d undergoes a sufficiently large number of low-frequency (i.e., breathing mode) oscillation cycles. Five sub-timesteps per ion timestep ($N_e = 5$) are used to integrate electron equations [19]. Time-averaged results shown here are averaged over several I_d cycles.

In order to assess the effects of the boundary conditions imposed at the downstream plume boundary P for the four plume domain sizes, a total of eight simulation cases are analyzed in this work, all of them featuring the same thruster operating point and general settings described above. Hereafter the different cases shall be referred to as P*i*L and P*i*G (see Table 2), where: $i = 1, 2, 3, 4$ indicates the corresponding plume domain size (i.e. P1 to P4); L refers to cases featuring the local zero net current condition at P in Eq. (16), and thus applying Eq. (17) for the electron energy flux at P with $c = 9/2$ [corresponding to $c_q = 2$ for the electron heat flux in Eq. (18)]; and G identifies cases applying the GDML model at P, described in Sec. II.A.

B. Assessment of the GDML effects on the 2D plasma discharge

This section analyzes the simulation results of the 2D plasma discharge obtained for the plume domain P2, taken as reference in this work. Cases P2L and P2G are compared in this section to address the effects of the boundary conditions applied at P.

The HYPHEN electron model requires the tuning of the turbulent function $\alpha_t(z, r)$ in Eq. (7) for the operation point to be simulated. Axial "step-out" profiles with two fitting parameters, α_{t1} and $\alpha_{t2}(> \alpha_{t1})$, applying, approximately, inside and outside the thruster chamber, respectively, have provided good fittings in previous studies [45–48]. In Ref. [22], experimental data for I_d and F guided the fitting of α_{t1} and α_{t2} for a 5kW-class HET prototype with magnetic shielding. Here, for the virtual HET, we take $\alpha_{t1} = 1.2\%$ and $\alpha_{t2} = 4.8\%$, both of the order of 10^{-2} [36], for all simulation cases in Table 2. Figure 2(e) shows the axial step-out profile used in this work for cases P2L and P2G. Along the thruster channel midline, the transition point $(\alpha_{t1} + \alpha_{t2})/2$ is located downstream the B peak, at $z/L_c = 1.49$. Table 3 summarizes the simulation results for all cases in Table 2, included here for completeness.

The simulation results capture well the so-called breathing mode [35, 49–51] that dominates the I_d oscillations. Figures 4(a) and 4(b) compare the time evolution of I_d and its normalized amplitude spectrum, respectively, for cases P2L and P2G. As expected, the boundary condition at P does not affect significantly the breathing mode, and both cases yield practically the same dynamic response. A large I_d oscillation is found, with peak values around four times the mean one. Table 3 lists the dominant breathing mode frequency f_d and the relative semi-amplitudes $\Delta I_d/I_d$ of the asymmetric I_d oscillations. The time-averaged thrust F in Table 3 is computed as the surface integral at P of the axial momentum flux of all plasma species leaving the simulation domain through P, being the ion contribution the main one (the contribution of electrons to thrust is 1.5% for P1 cases and less than 1% for cases P2-P4). Both P2L and P2G cases yield practically the same thrust values, indicating that the ion acceleration and downstream expansion in the near plume region is not significantly affected by the downstream boundary condition.

Figure 5 shows the time-averaged 1D axial profiles along the thruster channel midline of the neutral density n_n (including contributions of slow neutrals injected from the anode and cathode and emitted from the walls due to ion recombination there, and fast neutrals produced by CEX collisions), the plasma density n_e, the electric potential ϕ and the electron temperature T_e. Black solid and red dashed lines refer to cases P2G and P2L, respectively. Figure 6 depicts the time-averaged 2D (z,r) contours of the same plasma variables for cases P2L (left column) and P2G (right column). The results reveal that the main changes in these quantities, induced by the electron boundary condition at P, occur in the near plume region, while no significant differences in the plasma solution are reported inside the thruster chamber.

The neutral density inside the chamber is mainly shaped by the gas injection at the anode, the volume ionization and the neutral emission from the walls due to the ion recombination there. The neutral density decreases by a factor of about 35 along the chamber, where most of the ionization takes place. Figures 6(a)-(b) show the cathode neutral gas plume, which merges downstream with the one exiting the thruster chamber, yielding an increase neutral density

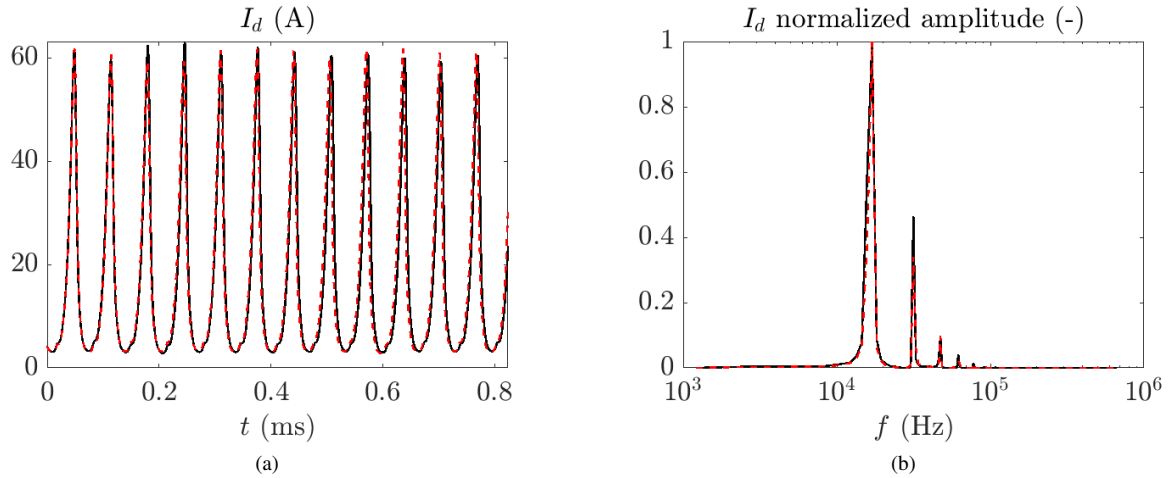

Fig. 4 (a) Time evolution of I_d. (b) I_d normalized amplitude spectrum. Black solid and red dashed lines correspond to cases P2G and P2L, respectively.

Case	F (mN)	I_d (A)	f_d (kHz)	$\Delta I_d/I_d$ (%)	T_{eP} (eV)	$\bar{T}_{eP}$ (eV)	ϕ_P (V)	$\bar{\phi}_P$ (V)	ϕ_∞ (V)
P1L	277.5	16.97	14.97	-82.4, 273.6	9.64	2.29	20.60	1.05	N/A
P2L	281.7	17.09	15.29	-81.8, 254.8	3.71	1.82	6.75	5.95	N/A
P3L	283.7	16.93	15.10	-82.2, 259.4	3.72	1.97	3.65	2.69	N/A
P4L	282.1	16.87	14.97	-82.4, 270.6	3.55	2.08	4.45	3.56	N/A
P1G	277.4	16.97	14.91	-83.8, 291.7	6.65	1.25	1.63	5.53	0.51
P2G	280.9	17.11	15.23	-82.0, 254.1	3.11	1.21	5.80	3.49	-1.70
P3G	281.6	16.88	15.02	-82.9, 263.1	3.29	1.41	3.49	2.07	-3.96
P4G	280.6	16.85	14.97	-82.6, 271.8	3.24	1.53	4.25	3.28	-2.94

Table 3 Time-averaged simulation results for all cases defined in Table 2. Values of F, I_d, dominant breathing mode frequency f_d and relative oscillation semi-amplitudes of I_d (negative and positive values refer to relative semi-amplitudes below and above the time-averaged I_d value, respectively). Values of the electron temperature and the electric potential at the intersection point between the P boundary and the thruster channel midline, T_{eP} and ϕ_P, respectively. The electron temperature and electric potential values averaged over the complete P boundary surface are $\bar{T}_{eP}$ and $\bar{\phi}_P$, respectively. Values of the infinity-to-cathode bias ϕ_∞.

downstream, as reveals Fig. 5(a). Figures 5(b) and 6(c)-(d) reveal a plasma density peak of about $1.7 \cdot 10^{18}$ m^{-3} at a central region of the chamber, close to the anode wall. In the near plume, n_e decreases due to ion acceleration and expansion. The natural particle reflection at the symmetry axis yields a higher plasma density there, thus giving rise to the formation of a single-peaked plasma plume downstream, as depicted in Figs. 6(c)-(d).

The axial potential fall inside the thruster chamber is about 30% of V_d, and most of the ion acceleration takes place in the region between the channel exit plane and the cathode magnetic line, depicted in green in Fig. 2(c), where equipotential lines follow approximately the magnetic lines. The region of maximum axial electric field, $E_z = -\partial\phi/\partial z$, extends from $z/L_c = 0.73$ to $z/L_c = 1.36$. Along the thruster channel midline ϕ falls down to 8.73 V and 8.09 V for cases P2L and P2G, respectively, at $z/L_c = 5.36$, where the cathode magnetic line crosses the thruster channel midline in the near plume region [refer to the green line in Fig. 2(c)]. These values represent estimations of the cathode coupling voltage [52].

The electron temperature peak is around 29 eV, and is located in the near plume, close to the channel exit, in the region of maximum axial electric field. Temperature isolines closely follow magnetic lines, and steep gradients are found upstream the T_e peak, where the electron flow enters into the thruster chamber, yielding values of about 6.5 eV around the anode wall. In the downstream plume boundary P, at the thruster channel mid radius, the electric potential is $\phi_P =$

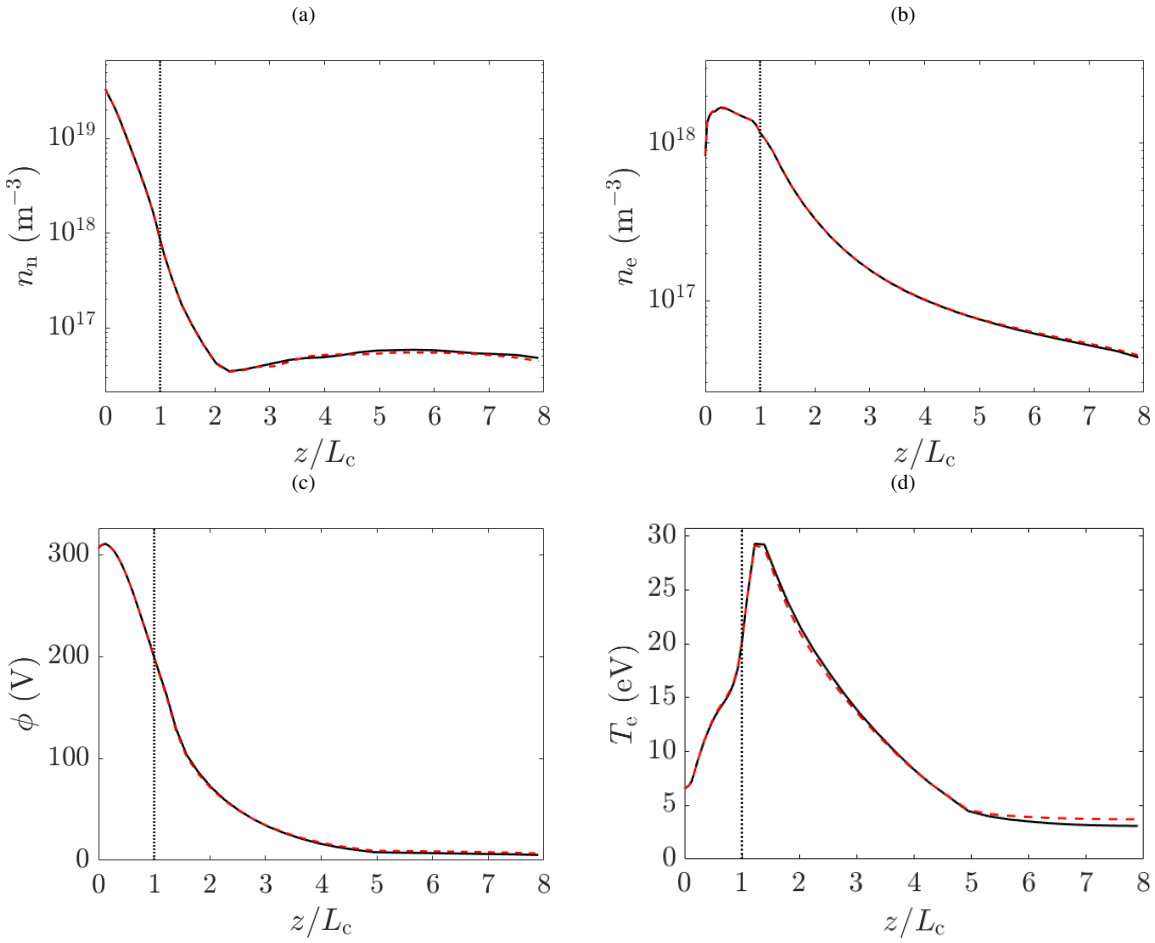

Fig. 5 Time-averaged 1D profiles along the thruster channel midline of (a) n_n, (b) n_e, (c) ϕ, and (d) T_e. Black solid and red dashed lines correspond to cases P2G and P2L, respectively. The vertical black dashed line indicates the thruster chamber exit plane.

5.80 V and 6.75 V for cases P2G and P2L, respectively. The electron temperature at those points is T_{eP} = 3.11 eV and 3.71 eV for cases P2G and P2L, respectively. Average values of the electric potential and the electron temperature over the P boundary, $\bar{\phi}_P$ and $\bar{T}_{eP}$, respectively, are listed in Table 3. The infinity-to-cathode bias for case P2G is ϕ_∞ = -1.70 V.

The time-averaged 2D maps of magnitude and streamlines of longitudinal (i.e., in-plane) ion $\tilde{\boldsymbol{j}}_i$ (including all ion species, i.e. produced from ionization of the neutral gas and from CEX collisions), electron $\tilde{\boldsymbol{j}}_e$ and electric $\tilde{\boldsymbol{j}}$ current densities (defined as $\tilde{\boldsymbol{j}}_i = \boldsymbol{j}_i - j_{\theta i}\mathbf{1}_\theta$ and so on) are shown in Fig. 7 for case P2L (left column) and P2G (right column). Most of the ionization of the neutral gas is distributed in the whole chamber volume. Ions, which are practically unmagnetized, follow the electric field, and are not prevented from impacting the channel walls. Plasma variables across the ionization and acceleration regions do not exhibit significant changes from case P2L to P2G. Since changes in the electric potential in the near plume region are much smaller than the average ion energy there, the ion flow is practically unaffected by the electron boundary conditions at P. The ion streamlines reveal the expected ion divergence, similar in both cases P2L and P2G, characterizing the beam expansion.

The cathode-born electron streamlines shown in Figs. 7(c)-(d) split into two electron beams: one flows downstream to neutralize the main ion beam, and the other progressively moves across the magnetic field into the thruster chamber to ionize the injected neutral gas and sustain the discharge. Part of this upstream electron flow, whose behavior is practically the same in both cases P2L and P2G, is collected to the lateral walls to cancel the ion flow and thus satisfy the dielectric condition imposed there. The simulation results reveal that the splitting of the cathode electron streamlines takes place along the cathode magnetic line, suggesting that the near plume domain should contain this closing magnetic line to properly capture the cathode-beam coupling and the neutralization of the ion beam exiting the thruster chamber.

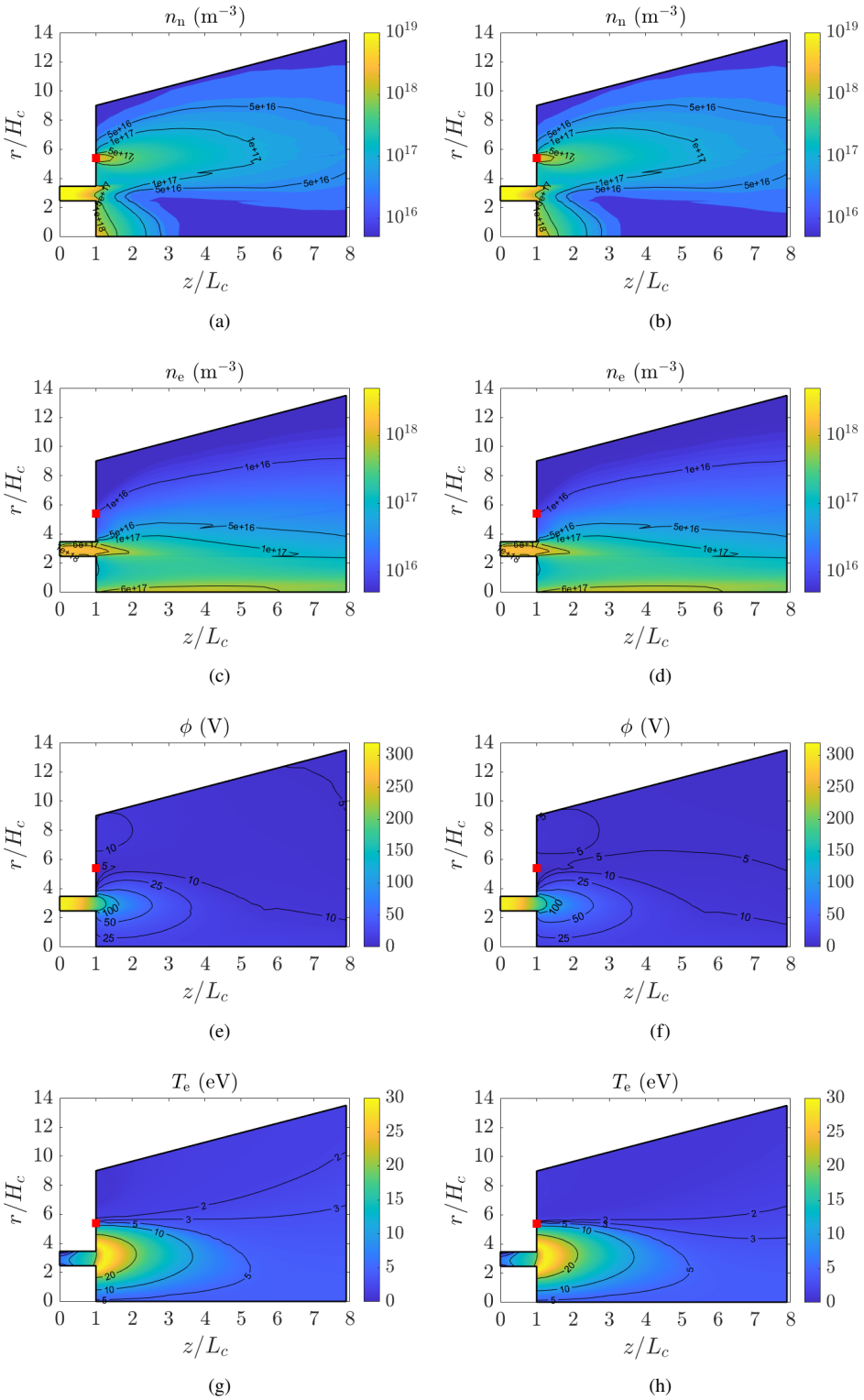

Fig. 6 Time-averaged 2D (z,r) contour maps for cases P2L (left column) and P2G (right column). (a)-(b) n_n, (c)-(d) n_e, (e)-(f) ϕ and (g)-(h) T_e. The red square marker indicates the cathode location.

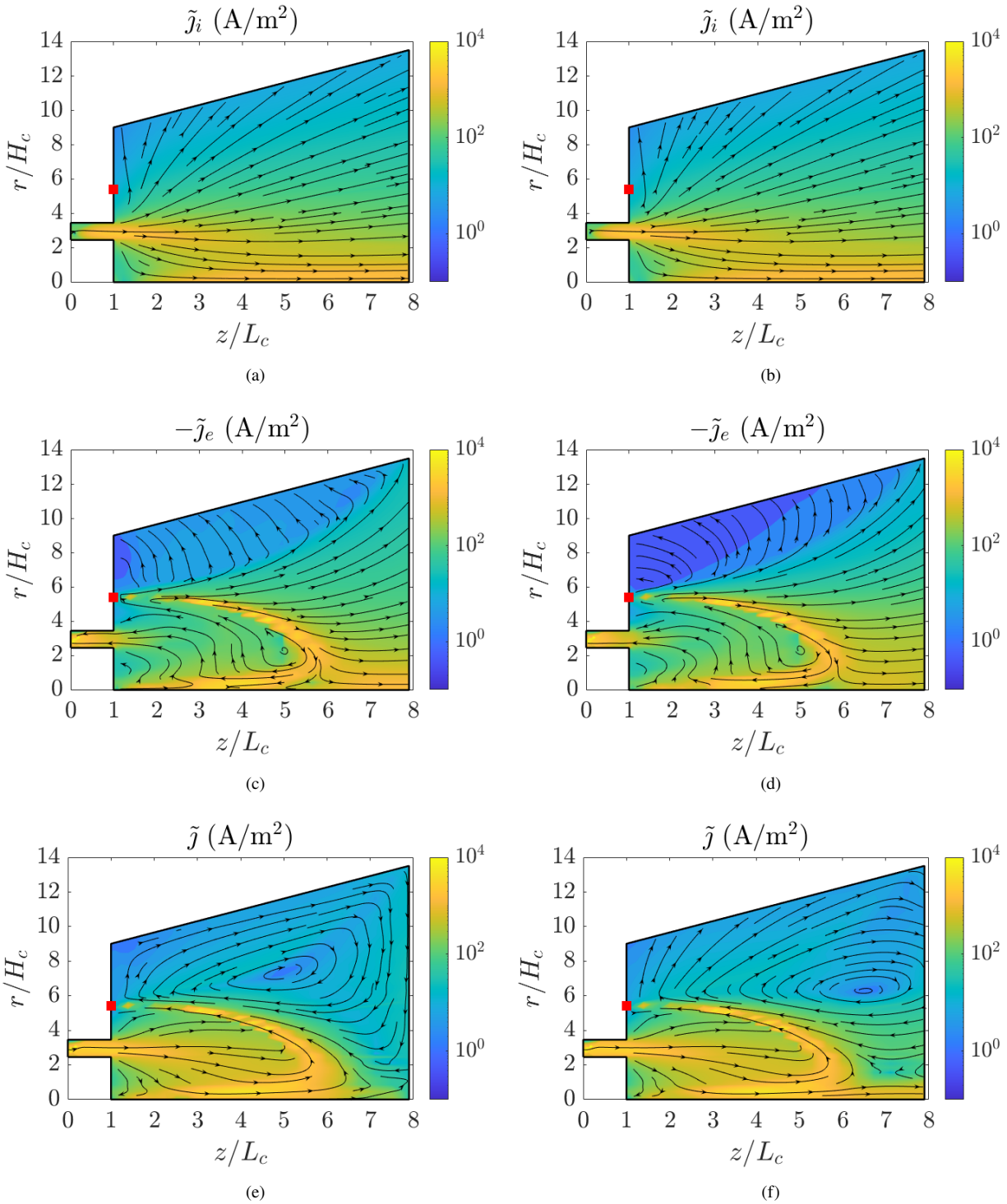

Fig. 7 Time-averaged 2D (z,r) contour maps for cases P2L (left column) and P2G (right column). Magnitude of (a)-(b) $\tilde{j}_i$, (c)-(d) $\tilde{j}_e$ and (e)-(f) $\tilde{j}$. Black lines with arrows depict the streamlines of (a)-(b) $\tilde{j}_i$, (c)-(d) $-\tilde{j}_e$ and (e)-(f) $\tilde{j}$. The red square marker indicates the cathode location.

Cases P1 do not satisfy this condition, as discussed below. The comparison of cases P2L and P2G reveals significant changes in the downstream, ion beam neutralizing electron flow. Compared to case P2L, the electron streamlines coming out the cathode in case P2G reveal a smoother transition of the electron flow towards the lateral plume boundary, following more closely the magnetic field lines there [refer to Fig. 2(c)]. This solution seems more representative of the still significantly magnetized electron population in the plume region simulated, where the average effective Hall parameter in Eq. (11) is $\sqrt{\chi\chi_t} \sim$ 70-250. Moreover, the decoupling between the local ion and electron current density at P yields a lower electron current collected at the lateral plume boundary, as discussed later. Figures 7(e)-(f) show the 2D streamlines of the longitudinal electric current for cases P2L and P2G, respectively. At the chamber lateral walls, the net electric current collected is locally null, and the ion flows are canceled by the electron ones. Both cases P2L and P2G present similar current loops connecting anode and cathode, as expected. However, the different solution for $\tilde{\boldsymbol{j}}_e$ downstream the cathode magnetic line in cases P2L and P2G affects the longitudinal electric current map in this region. The local null current condition at P in Eq. (16), imposed in case P2L, yields $\tilde{\boldsymbol{j}}$ streamlines parallel to P, as expected, and induces the development of a current loop fully contained in this region, with a $\tilde{\boldsymbol{j}} = \boldsymbol{0}$ point located at $z/L_c = 5.2$ and $r/H_c = 7.0$, as depicted in Fig. 7(e). On the other hand, the GDML model in case P2G decouples the local ion and electron currents collected at P, and a current loop closing at infinity develops downstream the cathode magnetic line, with the null current point now located at $z/L_c = 6.6$ and $r/H_c = 6.3$ as revealed in Fig. 7(f). Along P, the electric current locally leaves the domain where the ion current dominates over the electron one, mainly near the symmetry axis and along the lateral plume boundary, and flows into the domain along a central part of the axial plume boundary, thus assuring $I_\infty = 0$, as stated in Eq. (19).

To complete the results described above, Fig. 8 plots time-averaged values of ϕ_P, T_{eP}, j_{niP}, $-j_{neP}$, P''_{niP} and P''_{neP} along the downstream plume boundary P of the finite simulation domain. Black solid and red dashed lines correspond to cases P2G and P2L, respectively. The abscissa length s runs along P from the upper left corner to the bottom right corner of the plume domain. On each plot, the vertical black dotted line indicates the location of the upper right corner of the plume domain thus separating the lateral and axial boundaries of the plume domain. The vertical black dashed lines indicates the crossing point with the thruster channel midline.

Figure 8(c) confirms that the collected ion current profile at P is essentially the same in cases P2L and P2G so that, as discussed above, the ion expansion is practically unaffected by the electron boundary condition at P. The ion beam current leaving the simulation domain through P, obtained as the surface integral over P of the j_{niP} profiles in Fig. 8(c), is $I_{i\infty} = 15.3$ A, and around a 10% of it leaves the domain through the lateral boundary of the plume domain in both cases, being mainly carried by high-divergence fast ions and slow CEX ions generated in the core of the ion beam exiting the thruster chamber. The contribution of CEX species to the ion current leaving the simulation domain through the lateral boundary of the plume is about 3%.

While in case P2L the distribution along P of the electron current density leaving the simulation domain follows that of the ion population according to Eq. (16), in case P2G the GDML model locally decouples j_{neP} from j_{niP}. In this case, the local j_{neP} values are mainly controlled by the local ratio $e\phi_{\infty P}/T_{eP} \sim$ 2.4-6.5, with $\phi_{\infty P}$ the P-to-infinity local potential drop (refer to Sec. II.A). As shown in Fig. 8(d), a significantly different j_{neP} distribution along P is obtained in this case, while the surface integral over P of $j_{nP} = j_{neP} + j_{niP}$ yields $I_\infty = 0$, according to Eq. (19). In case P2G, the total electron current leaving the simulation domain through the lateral plume boundary amounts to about 4% of $I_{i\infty}$ only. The different j_{neP} distribution in cases P2L and P2G affects the electric potential profile along P, shown in Fig. 8(a), which is locally adjusted to satisfy current continuity in Eq. (2) at the MFAM boundary cells. Compared to case P2G, case P2L features higher ϕ_P values, especially along the lateral boundary of the plume domain [refer also to Figs. 6(e)-(f)], where a higher P-to-cathode bias is required to extract a larger electron current, locally equal to the ion one.

Figure 8(e) plots the profiles of the ion energy flux at the quasineutral boundary P (i.e., it does not include the additional ion energy gain in the thin downstream matching layer), P''_{niP}, for cases P2L and P2G. This magnitude is computed directly by the I-module (refer to the Appendix) considering all ion species simulated, including singly and doubly fast and CEX (i.e., slow) ions, and confirms that the energy content of the ion beam is not affected by the electron boundary condition at P. As expected, the ion energy flux at P is about 1-2 orders of magnitude larger than the electron one, P''_{neP}, shown in Fig. 8(f) for both cases. For case P2L, P''_{neP} is given by Eq. (17) with $c = 4.5$, so that the ratio $eP''_{neP}/(j_{neP}T_{eP})$ is constant. On the other hand, for the case P2G, P''_{neP} is given by Eq. (21), and depends on the local ratio $e\phi_{\infty P}/T_{eP}$. The resulting electron temperature along P is lower than that of case P2L along most of the downstream plume boundary, as shown in Fig. 8(b), with $eP''_{neP}/(j_{neP}T_{eP}) \sim$ 4.4-8.5.

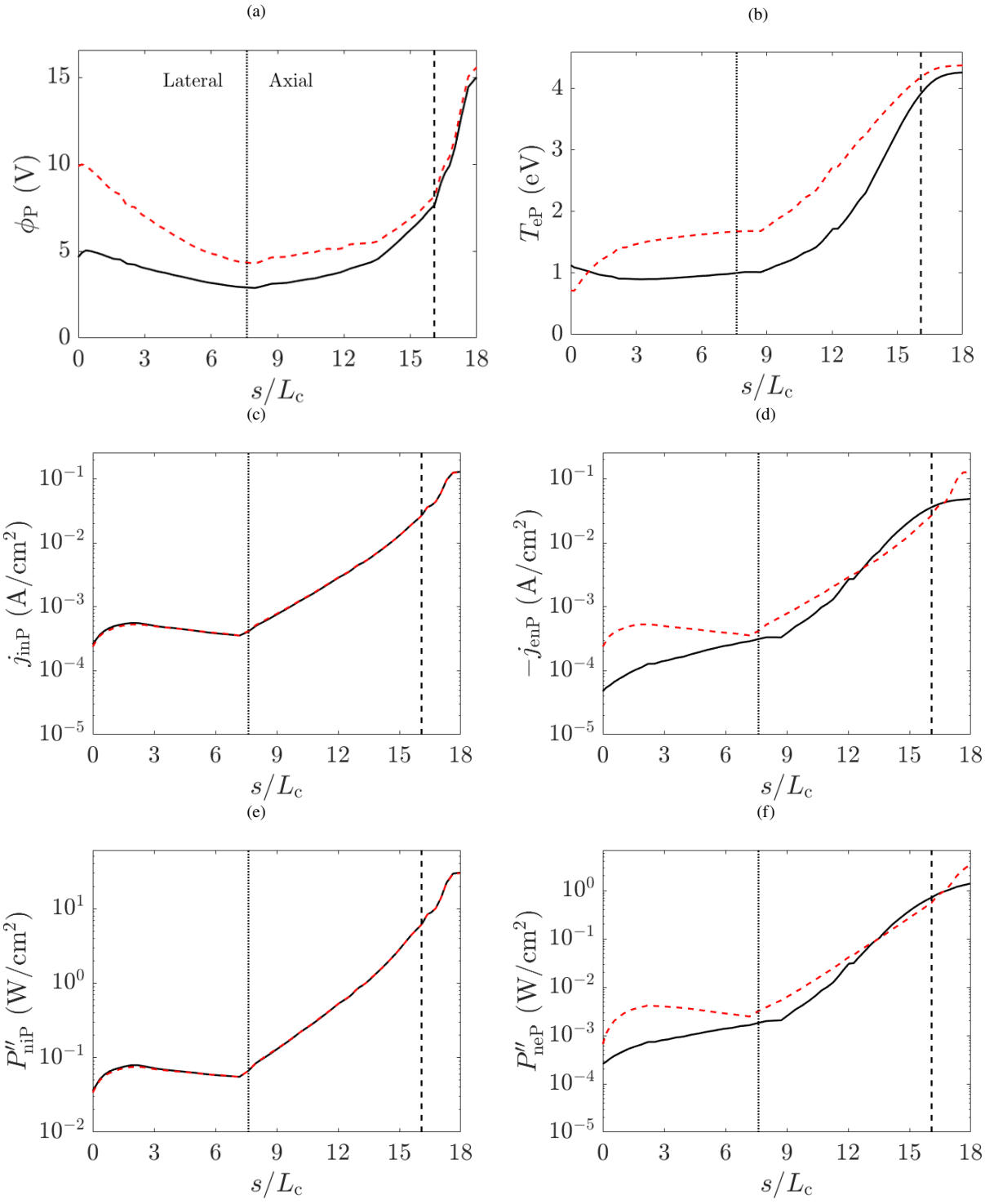

Fig. 8 Time-averaged profiles along the downstream plume boundary P of (a) ϕ_{P}, (b) T_{eP}, (c) j_{niP}, (d) $-j_{\mathrm{neP}}$, (e) P''_{niP} and (f) P''_{neP}. Black solid and red dashed lines correspond to cases P2G and P2L, respectively. Coordinate s runs along P, with $s = 0$ at the upper left corner of the plume domain. The vertical black dotted line indicates the location of the upper right corner of the plume domain, separating the lateral and axial plume boundaries, while the vertical black dashed line indicates the crossing point with the thruster channel midline.

C. Analysis of current and power balances and performances

The stationary ion current and the plasma power balances are analyzed in this section, focusing on cases P2L and P2G. Simulation results for all cases in Table 2 are included for completeness. Considering all ion species simulated, the ion current balance at steady state is

$$I_{\text{prod}} = I_{\text{i}\infty} + I_{\text{iD}} + I_{\text{iA}} + I_{\text{iC}}, \tag{23}$$

where I_{prod} is the total ion current generated by ionization in the simulation domain; I_{iD}, I_{iA} and I_{iC} are the ion currents impacting the dielectric, anode and cathode walls, respectively; and $I_{\text{i}\infty}$ is the ion beam current leaving the domain through P, which is the only one contributing to thrust. All currents are defined as positive. While I_{prod} is obtained from a volumetric integration, all the other ones are computed from surface integrals at the corresponding domain boundaries.

Case	I_{prod} (A)	$I_{\text{i}\infty}/I_{\text{prod}}$	$I_{\text{iD}}/I_{\text{prod}}$	$I_{\text{iA}}/I_{\text{prod}}$	η_{u}	η_{cur}	η_{ch}
P1L	21.10	0.72	0.20	0.08	0.92	0.89	0.84
P2L	21.25	0.72	0.21	0.07	0.93	0.90	0.85
P3L	21.17	0.72	0.20	0.08	0.93	0.90	0.85
P4L	21.03	0.72	0.20	0.08	0.93	0.90	0.85
P1G	21.07	0.72	0.20	0.08	0.92	0.89	0.85
P2G	21.20	0.72	0.21	0.07	0.93	0.89	0.85
P3G	21.18	0.72	0.20	0.08	0.93	0.90	0.85
P4G	20.97	0.72	0.20	0.08	0.93	0.90	0.85

Table 4 Value of I_{prod} and fractions of I_{prod} corresponding to the different contributions to the current balance in Eq. (23). Values of η_{u}, η_{cur} and η_{ch}, defined in Eq. (24).

Case	P (kW)	η	P_{inel}/P	P_{D}/P	P_{A}/P	P_{∞}/P $(=\eta_{\text{ene}})$	η_{div}	η_{disp}
P1L	5.16	0.39	0.08	0.21	0.05	0.66	0.76	0.79
P2L	5.19	0.40	0.08	0.21	0.06	0.65	0.77	0.81
P3L	5.14	0.41	0.08	0.20	0.06	0.66	0.77	0.81
P4L	5.13	0.41	0.08	0.21	0.06	0.65	0.78	0.81
P1G	5.16	0.39	0.08	0.20	0.06	0.66	0.76	0.78
P2G	5.20	0.40	0.08	0.21	0.06	0.65	0.77	0.80
P3G	5.13	0.41	0.08	0.20	0.06	0.66	0.77	0.81
P4G	5.12	0.41	0.08	0.21	0.06	0.65	0.78	0.81

Table 5 Value of P and fractions of P corresponding to different contributions to the power balance in Eq. (25). Values of η, η_{ene}, η_{div} and η_{disp}, defined in Eqs. (26) and (27).

Table 4 lists I_{prod} and the fractions collected at the different boundaries for the different simulation cases. The value of I_{iC} is about one order of magnitude lower than I_{iA} for all simulation cases and has not been included. The results reveal that for all cases, a 28% of the produced ion current is collected at the thruster chamber walls, while the remaining 72% leaves the domain through P, contributing to thrust (the produced thrust is practically the same for all cases, as listed in Table 3, and is mainly due to ions, the electron contribution to thrust being lower than 1% for all cases). Table 4 also includes the propellant utilization, the current efficiency, and the charge efficiency, defined as

$$\eta_{\text{u}} = \frac{\dot{m}_{\text{i}\infty}}{\dot{m}}, \qquad \eta_{\text{cur}} = \frac{I_{\text{i}\infty}}{I_{\text{d}}}, \qquad \eta_{\text{ch}} = \frac{e\dot{m}_{\text{i}\infty}}{m_{\text{i}} I_{\text{i}\infty}}, \tag{24}$$

respectively. Here $\dot{m} = \dot{m}_{\text{A}} + \dot{m}_{\text{C}}$, $\dot{m}_{\text{i}\infty}$ is the total ion mass flow across the plume boundaries, and $\eta_{\text{ch}} = 1$ if all ions are singly charged. The values of η_{u} and η_{cur} are rather good compared to typical HET operation values (η_{cur} ~0.6-0.8 [53]). Similar current ratios and η_{u}, η_{cur} and η_{ch} values are found for all cases.

The plasma power balance for the steady state discharge is

$$P = P_\infty + P_\mathrm{D} + P_\mathrm{A} + P_\mathrm{inel}, \tag{25}$$

where: $P = I_\mathrm{d}V_\mathrm{d} + P_\mathrm{C}$ is the total power deposited into the plasma discharge, which is the sum of the discharge power, $P_\mathrm{d} = I_\mathrm{d}V_\mathrm{d}$, and the net power delivered through cathode electron emission, P_C, amounting to 1-2% of P; P_∞ is the plasma energy flow through the downstream plume boundary P; P_D and P_A are the power losses at the dielectric walls and at the anode wall, respectively; and P_inel corresponds to the power losses due to inelastic (e.g., ionization and excitation) collisions. All powers are defined as positive. The value of P_inel is obtained from a volumetric integral; P_∞, is computed from the surface integral at the downstream plume boundary P (the integral of P''_niP and P''_neP yields the contribution of ions and electrons, respectively); and the values of P_D and P_A come from surface integrals at the respective walls (not at the Debye sheath edges).

The thrust efficiency is defined and factorized as

$$\eta = \frac{F^2}{2\dot{m}P} \equiv \eta_\mathrm{ene}\eta_\mathrm{div}\eta_\mathrm{disp}, \tag{26}$$

where the energy, divergence, and dispersion efficiencies are defined, respectively, as

$$\eta_\mathrm{ene} = \frac{P_\infty}{P} \qquad \eta_\mathrm{div} = \frac{P_{z\infty}}{P_\infty}, \qquad \eta_\mathrm{disp} = \frac{F^2}{2\dot{m}P_{z\infty}}, \tag{27}$$

with $P_{z\infty}$ the flow of axial plasma energy across P. In Eq. (27), η_ene quantifies the relative power in the downstream plume, η_div assesses the plume divergence based on axial energy and total energy flows, and η_disp quantifies the level of velocity dispersion of all plasma species (which would be one for a mono-velocity gas). Plume energy flows P_∞ and $P_{z\infty}$ include the corresponding electron contribution, due to their incomplete expansion in the finite simulation domain. This residual electron energy accounts for about 13% of P_∞ for P1 cases, and ranges around 4-7% for the other cases, slightly decreasing for larger plume domains, as expected.

Table 5 lists the contributions to the power balance in Eq. (25) and the values of the efficiencies in Eqs. (26) and (27). Similar results are obtained for all simulated cases, revealing a slight effect of the electron boundary condition at P, and of the plume domain extension, on the overall thruster performance. The plasma losses to the chamber walls amount up to a 26-27% of the input power (most of them deposited at the lateral dielectric walls). The effective single ionization cost is $P_\mathrm{inel}/I_\mathrm{prod} \sim 20$ eV, including the contribution from excitation collisions. The energy efficiency, η_ene, which is a plasma source related efficiency measuring the fraction of the input power transmitted to the plume, is about 66% for all cases, and thus is not affected by the plume size, as expected. For the case of a virtual EPT, the plume-related efficiencies η_div and η_disp have been shown to increase about a 10% with the plume size due to the incomplete beam expansion in the divergent magnetic nozzle outside the thruster vessel [14]. Here, no significant electron cooling is found downstream the cathode magnetic line (discussed below) and the electron temperature at P remains similar for P2-P4 cases (refer to values in Table 3). As a result, η_div and η_disp remain nearly constant with the plume size, limiting the thrust efficiency to around 40% (the anodic thrust efficiency, considering only the anode propellant mass flow is about 43%) for all cases. As listed in Table 3, thrust variations among cases are below 3%. Setting $\cos^2\alpha_\mathrm{div} = \eta_\mathrm{div}$, the half-divergence angle in the plume is $\alpha_\mathrm{div} \sim 28.0$-29.3 deg.

D. Plume extension analysis

As described in Secs. III.B and III.C, all the simulation cases in Table 2 feature a similar plasma solution inside the thruster chamber, including the breathing mode dynamics. Also, only slight variations in the overall discharge performance figures have been found, as listed in Tables 3, 4 and 5. In this section, the plasma solution in the near plume for all cases in Table 2 is compared to address the effects of the electron boundary conditions at P on relevant plasma properties for different plume domain sizes.

Figure 9 shows axial profiles of ϕ, T_e, and n_e along the thruster channel midline in the near plume region, from $z/L_\mathrm{c} = 3$ up to the downstream plume boundary P for cases P1L-P4L (left column) and cases P1G-P4G (right column). As expected, the electron boundary conditions at P have a larger effect on P1 cases, for which the cathode magnetic line [refer to the green line in Fig. 2(c)] is not fully contained within the simulation domain and crosses the downstream plume domain, clearly affecting the cathode-beam coupling. On the other hand, P4 cases present very similar ϕ, T_e, and n_e profiles, indicating that the electron boundary conditions at P induce rather marginal effects on the bulk plasma

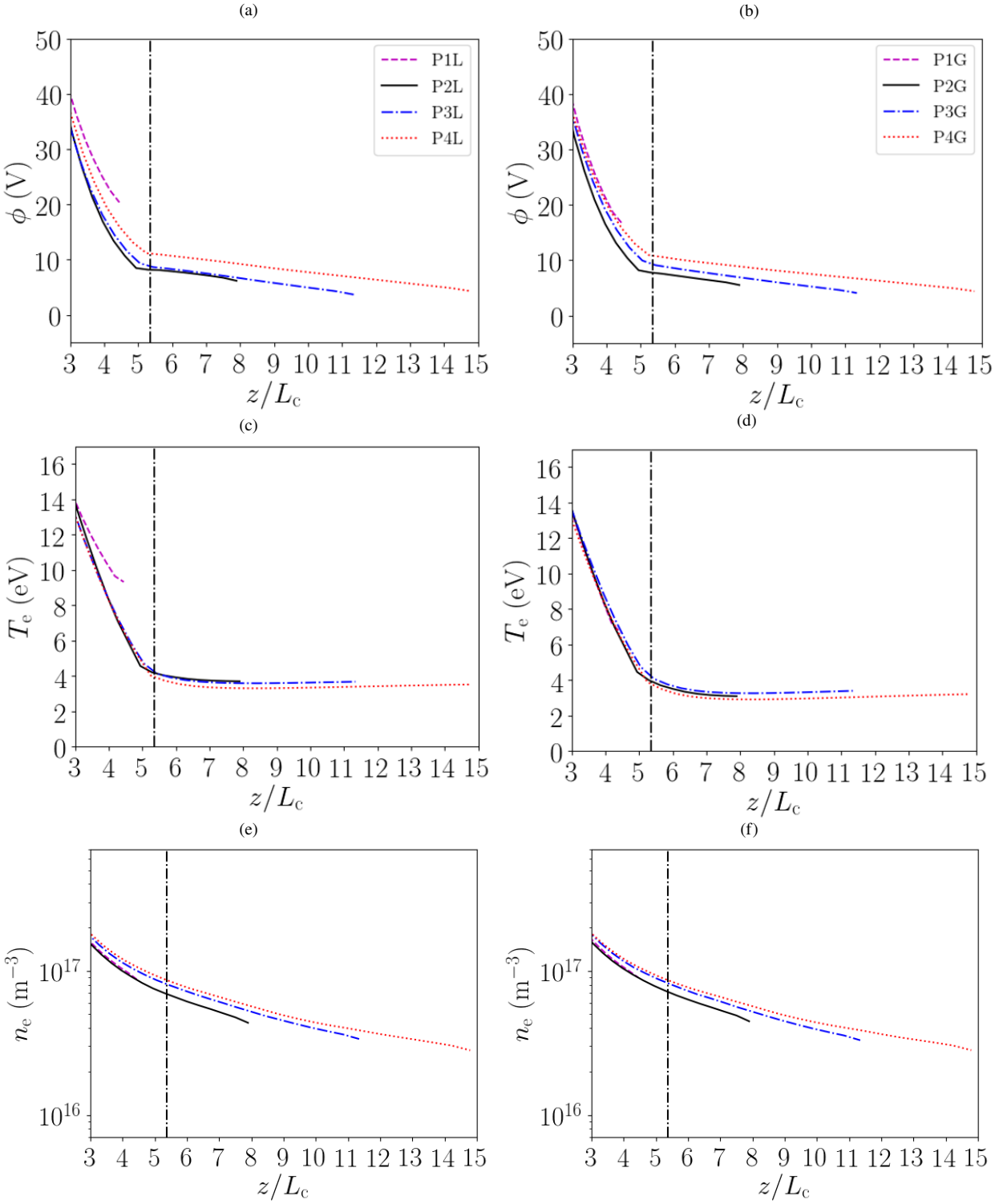

Fig. 9 Time-averaged 1D axial profiles along the thruster channel midline in the near plume region for cases P1L-P4L (left column) and cases P1G-P4G (right column). (a)-(b) ϕ, (c)-(d) T_e and (e)-(f) n_e. The vertical black dot-dashed line indicates the crossing point with the cathode magnetic line at $z/L_c = 5.36$.

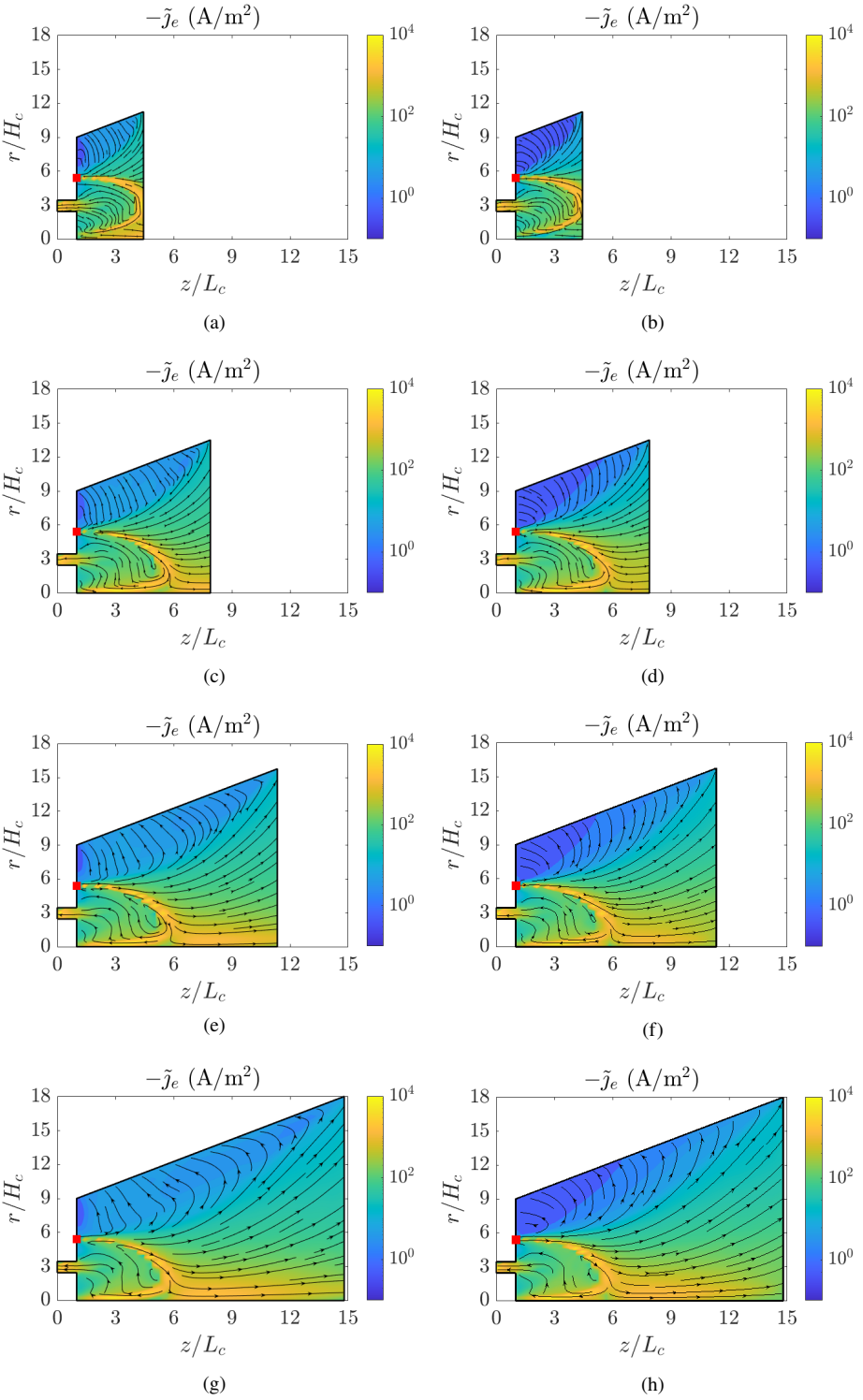

Fig. 10 Time-averaged 2D (z,r) contour maps of $-\tilde{j}_e$ for cases P1L-P4L (left column) and P1G-P4G (right column). The red square marker indicates the cathode location.

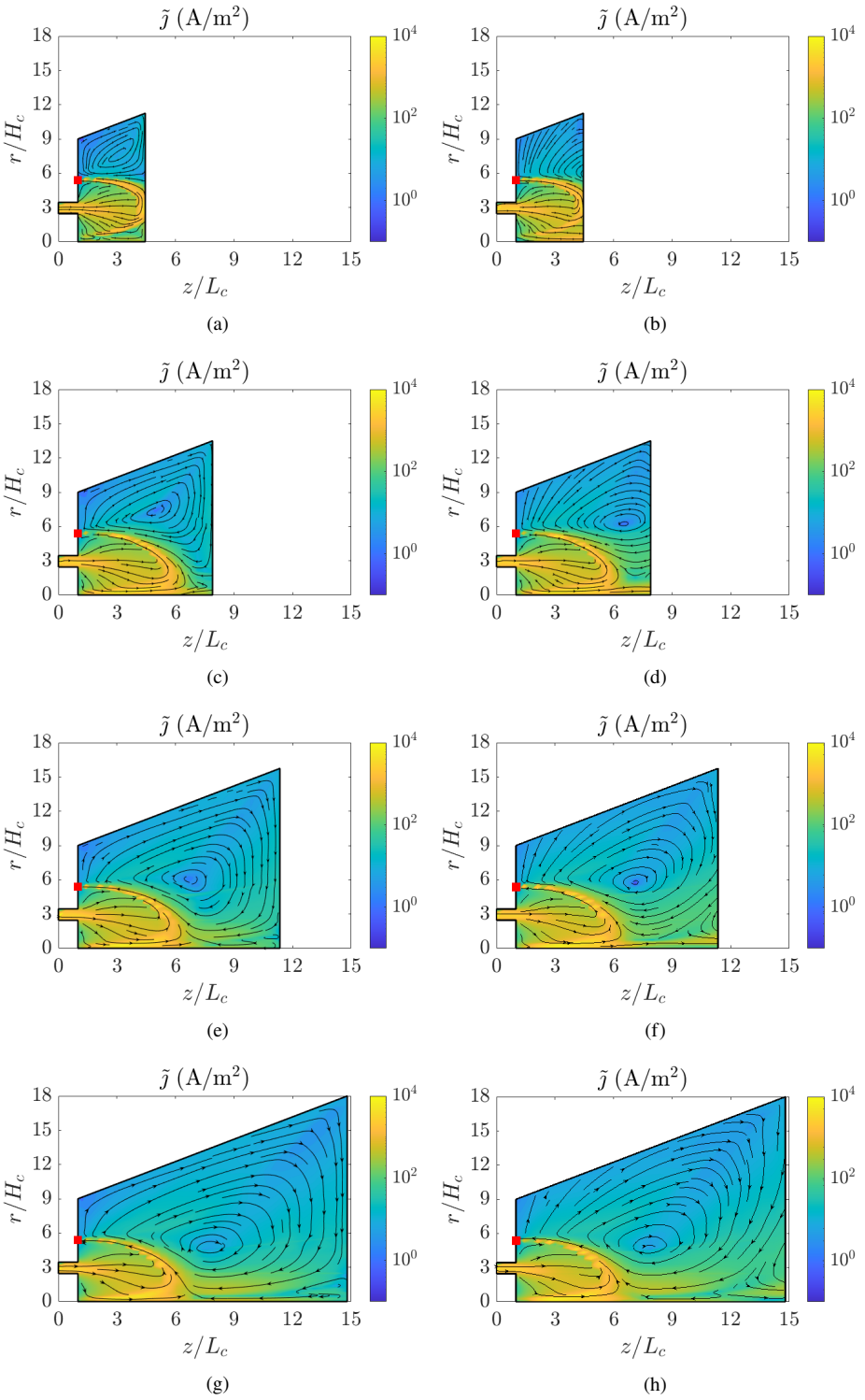

Fig. 11 Time-averaged 2D (*z*,*r*) contour maps of $\tilde{j}$ for P1L-P4L cases (left column) and P1G-P4G cases (right column). The red square marker indicates the cathode location.

solution for larger plume sizes. Compared to case P1G, the solution for ϕ and T_e in case P1L presents larger deviations with respect to that of P4 cases. Similar axial profiles are found for intermediate plume size P2 and P3 cases. Differences in the axial ϕ profile arise upstream the crossing point with the cathode magnetic line, indicated in Fig. 9 by the vertical black dot-dashed lines at $z/L_c = 5.36$, yielding slightly different cathode coupling voltages. Compared to case P4, maximum differences in the cathode coupling voltage for cases P2 and P3 range around 1% of V_d. For $z/L_c > 5.36$, $E_z = -\partial\phi/\partial z$ is practically identical for all cases, corresponding to nearly parallel ϕ profiles. The electron temperature remains nearly constant for $z/L_c > 5.36$ for all cases, and no significant electron cooling is observed. Table 3 gathers values of ϕ_P and T_{eP} corresponding to the final point of the profiles, where the thruster channel midline crosses the P boundary, along with average values of these quantities over the P boundary, $\bar{\phi}_P$ and $\bar{T}_{eP}$. For cases P1G-P4G, a similar ratio $e\bar{\phi}_{\infty P}/\bar{T}_{eP} = 4.0$-$4.3$, averaged over P, is found. This is consistent with the slight differences found in both the net axial electric potential drop accelerating the ion flow (similar thrust values are listed in Table 3 for all cases) and the electron temperature solution in the near plume region among cases P1G-P4G. Values of the infinite-to-cathode bias ϕ_∞ are listed in Table 3, ranging about 0.2-1.3% of V_d. While a positive ϕ_∞ is obtained in case P1G, in which the current neutralization in the plume region is more affected by the plume boundary, negative values are found for P2G-P4G cases.

A slightly higher plasma density profile is obtained for larger plume domain sizes from P2 to P4. Since the propellant utilization is practically the same for all cases, this fact indicates a slightly lower ion beam acceleration for larger plume sizes, which is consistent with their corresponding higher coupling voltage.

Figures 10 and 11 compare the time-averaged 2D maps of magnitude and streamlines of longitudinal electron $\tilde{\boldsymbol{j}}_e$ and electric $\tilde{\boldsymbol{j}}$ current densities for cases P1L-P4L (left column) and P1G-P4G (right column). The results for the ion longitudinal current density $\tilde{\boldsymbol{j}}_i$ show no significant differences among simulated cases and have been omitted for simplicity. Therefore, for all cases, the effects of the electron boundary condition at P on the solution for $\tilde{\boldsymbol{j}}$ are due to changes in $\tilde{\boldsymbol{j}}_e$ among the simulated cases. As described in Sec. III.B, the cathode-born electron flow splits into an upstream fraction moving into the thruster chamber and a downstream ion beam neutralizing one. In cases P2-P4 this splitting takes place along the cathode magnetic line [refer to the green line in Fig. 2(c)] yielding a similar solution for the longitudinal electron and electric currents upstream this magnetic line. However, in cases P1, the axial downstream plume boundary cuts the cathode magnetic line and forces the cathode electron flow to split along magnetic lines which are enclosed by the one corresponding to the cathode, thus significantly affecting the plasma solution and the cathode-beam coupling and current neutralization in this region, as discussed above.

Regarding the downstream ion beam neutralizing electron flow, for each plume domain size, differences in the solution for $\tilde{\boldsymbol{j}}_e$, shown in Fig. 10, induced by the electron boundary condition imposed at the downstream plume boundary P for L and G cases, are qualitatively the same as those found for cases P2L and P2G, discussed in Sec. III.B. As depicted in Fig. 11, the electron boundary condition imposed at P affects mainly the neutralization of the ion beam current downstream the cathode magnetic line. The simulation results reveal that the solution for $\tilde{\boldsymbol{j}}$ in this region is significantly more affected by the plume size in L cases, in which the local null current condition at P imposes the longitudinal electric current streamlines to be parallel to P, thus forcing the development of a current loop fully contained within the plume domain. As expected, a similar $\tilde{\boldsymbol{j}}$ solution in the bulk plume domain is obtained in P4 cases, indicating that the local null current condition is only a good approximation for sufficiently large plume simulation domains. In both P4L and P4G cases, the null electric current point in the bulk plume domain downstream the cathode magnetic line is located at $z/L_c = 7.8$, $r/H_c = 4.8$. A larger variation of the location of this point is found for L cases compared to G cases. For P2L, it is located at $z/L_c = 5.2$ and $r/H_c = 7.0$, thus yielding a 33% and 46% axial and radial change, respectively, when compared to P4 cases. On the other hand, in G cases, decoupling j_{neP} from j_{niP} reduces the effect of the plume size on the solution for $\tilde{\boldsymbol{j}}$. In cases P1G to P4G, a similar current loop closing at infinity develops downstream the cathode magnetic line. With respect to P4 cases, the position of the $\tilde{\boldsymbol{j}} = \boldsymbol{0}$ point for case P2G features a 15% and 31% axial and radial change, respectively, yielding $z/L_c = 6.6$ and $r/H_c = 6.3$. Therefore, the results indicate that the GDML model limits the influence of the plume domain size on the ion beam neutralization downstream, and provides a more robust solution for $\tilde{\boldsymbol{j}}$ in the near plume region against the plume truncation, thus increasing the reliability of the simulation results for smaller, less computationally demanding plume domains. Compared to P4 cases, P2 cases are around 22% faster in a single core run.

Finally, Fig. 12 compares the radial profiles of $j_{zi} = \boldsymbol{j}_i \cdot \boldsymbol{1}_z$ and $j_{ze} = \boldsymbol{j}_e \cdot \boldsymbol{1}_z$ at $z/L_c = 7.9$ (i.e., axial downstream plume boundary of P2 cases) for cases P2L-P4L (left column) and P2G-P4G (right column). The results in Figs. 12(a)-(b) confirm that the ion expansion is essentially the same for all cases, being practically unaffected by the electron boundary condition at P, as discussed above. Focusing on Figs. 12(c)-(d), the results for P2 cases (black solid lines) refer to j_{ne} values imposed by the corresponding boundary condition, since the outward unit normal vector along the axial plume boundary is $\boldsymbol{1}_n = \boldsymbol{1}_z$. The comparison with the profiles of j_{ze} for cases P3 and P4 reveals that the boundary

condition at P (both the local null current and the GDML model) affects the electron axial flow in the plume, and it is not able to reproduce the results obtained for larger plume sizes in cases P3 and P4. The largest discrepancies are found in the outer part of the plume, for $r/H_c \sim 10$ and $r/H_c \sim 12$ for L and G cases, respectively, where the boundary condition at P in P2 cases cannot reproduce the values $u_{ze} < 0$ obtained for cases P3 and P4, as indicated by the streamlines of the longitudinal electron current in Figs. 10(e)-(h) (electron streamlines refer to $-\tilde{\boldsymbol{j}}_e = en_e\tilde{\boldsymbol{u}}_e$, thus indicating the electron macroscopic paths in the half meridian 2D (z,r) plane). In Figs. 12(c)-(d), corresponding negative values of $-j_{ze} = en_e u_{ze}$ have been plotted in absolute value. In any case, the electron current in these regions is around 2-3 orders of magnitude smaller than in the mid radius of the thruster chamber.

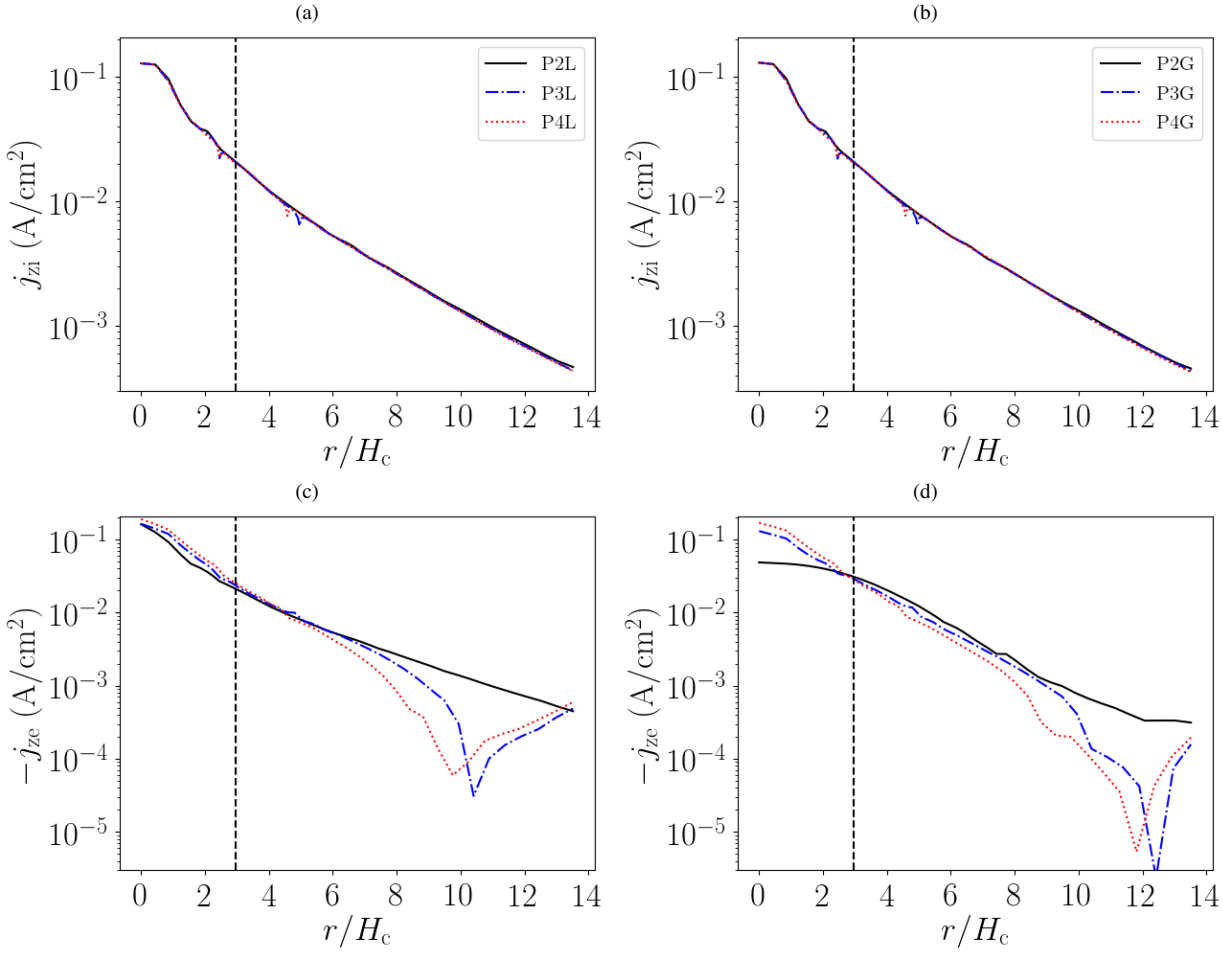

Fig. 12 Time averaged 1D radial profiles at $z/L_c = 7.9$ (i.e., axial downstream plume boundary of P2 cases) for cases P2L-P4L (left column) and P2G-P4G (right column). (a)-(b) j_{zi}, (c)-(d) $-j_{ze}$. The vertical black dashed line indicates the crossing point with the thruster channel midline. In (c) and (d), negative values of $-j_{ze} = en_e u_{ze}$ for $r/H_c \sim 10$ and $r/H_c \sim 12$, respectively, have been plotted in absolute value.

IV. Conclusion

HYPHEN numerical simulations of a 5kW-class HET plasma discharge for different electron boundary conditions imposed at the quasineutral plume boundary P of the simulation domain have been presented in this work. The local null current condition, typically imposed at P, has been compared against a new GDML model for the plume expansion to infinity, which assures a globally current-free plasma plume, estimates the final electric potential in the plume, and provides expressions for the electron particle and energy fluxes to be imposed as boundary conditions for the quasineutral electron fluid model of the hybrid HET discharge simulator.

The simulation results reveal that the electron boundary conditions imposed at P affect mainly the cathode-born

ion beam neutralizing downstream electron flow, while the anode-to-cathode plasma discharge, including the plasma solution inside the thruster chamber and in the very near plume region, enclosed by the cathode magnetic surface, is not significantly affected by the electron boundary conditions imposed at P, nor by the size of the plume region simulated, and similar discharge performance are found for all cases presented in this work. The largest discrepancies are obtained for the shortest plume domain simulated (P1 cases), for which the axial plume domain boundary cuts the cathode magnetic line, thus significantly affecting the cathode-beam coupling and current neutralization in the plume.

While the expansion of the ion beam exiting the thruster chamber is practically unaffected by the plume size and the electron boundary conditions imposed at P, the latter greatly affects the electron flow downstream the cathode magnetic line. Contrary to the null local current condition, the GDML model locally decouples ion and electron currents leaving the domain through P, and provides an electron current solution in the bulk plume domain that seems more representative of the still magnetized electron population in the near plume region, with electron streamlines following more closely the magnetic field lines there. The corresponding electric current solution is found to be more robust against the size of the near plume region simulated, indicating that GDML model limits the influence of the plume domain size on the ion beam neutralization downstream. Therefore it increases the reliability of the simulation results obtained for smaller, less computationally demanding plume domains. As expected, a similar electric current solution in the bulk plume domain is obtained for the largest plume domain size simulated, indicating that the local null current condition is only a good approximation for sufficiently large plume simulation domains.

All simulated cases feature a similar electron temperature solution in the plume region. No relevant electron cooling downstream the cathode magnetic line is observed, and rather small variations are found among cases for the far plume final electric potential (with respect to cathode). Future work will assess the performance of the GDML model when applied to plasma discharges of novel EPT technologies under development, featuring a divergent magnetic nozzle configuration in the plume. Additionally, further work will investigate the effects of phenomenological parallel-field electron cooling models in the plume.

Appendix. The sheath model

The S-module relates plasma magnitudes at the quasineutral Debye sheath edge Q and at the wall W, providing the appropriate boundary conditions for the quasineutral electron fluid equations in terms of j_{ne} and P''_{ne} at each quasineutral MFAM boundary face (i.e. Debye sheath edge Q). A planar, unmagnetized, collisionless, kinetic model is considered for the thin Debye sheaths developing around the walls. The model includes SEE and retains other non-Maxwellian features of the electron VDF [54].

Considering a dielectric wall (ceramic material with large SEE), the electric current density of primary (p) electrons collected at the wall from the quasineutral plasma is

$$j_{\mathrm{np}}(\phi_{\mathrm{WQ}}) = -(1-\delta_{\mathrm{r}})\sigma_{\mathrm{rp}} e \frac{n_{\mathrm{eQ}}\bar{c}_{\mathrm{eQ}}}{4} \exp\left(\frac{-e\phi_{\mathrm{WQ}}}{T_{\mathrm{eQ}}}\right), \tag{28}$$

which corresponds to a partially-depleted, partially-reflected Maxwellian VDF [54], and where ϕ_{WQ} is the potential fall in the sheath, $\bar{c}_{\mathrm{eQ}} = \sqrt{8T_{\mathrm{eQ}}/(\pi m_{\mathrm{e}})}$, δ_{r} is the fraction of elastically reflected primary electrons in the sheath, and σ_{rp} models the replenishment fraction of the VDF tail corresponding to impacting electrons. The net, local wall-collected electron current density is

$$j_{\mathrm{ne}} = j_{\mathrm{np}}(1-\delta_{\mathrm{s}}), \tag{29}$$

with δ_{s} the SEE yield. Kinetic studies of plasma-wall interaction [55–57] show that $\sigma_{\mathrm{rp}} < 1$ because of the weak electron collisionality. Here we take $\sigma_{\mathrm{rp}} = 0.3$.

For a conducting wall, such as the anode, we just take $\delta_{\mathrm{s}},\ \delta_{\mathrm{r}} = 0$. For the lateral ceramic walls, δ_{r} and δ_{s} are modeled according to [54, 58–61]

$$\delta_{\mathrm{r}}(T_{\mathrm{eQ}}) = \delta_{\mathrm{r0}} E_{\mathrm{r}}^2 / \left(T_{\mathrm{eQ}} + E_{\mathrm{r}}\right)^2, \tag{30}$$

$$\delta_{\mathrm{s}}(T_{\mathrm{eQ}}) = \min\left(2T_{\mathrm{eQ}}/E_1, \delta_{\mathrm{s}}^*\right), \tag{31}$$

with δ_{r0}, E_{r} and E_1 being material dependent parameters, and δ_{s}^* the effective upper-bounded SEE yield, corresponding to a space-charge limited (SCL) sheath with $e\phi_{\mathrm{WQ}}/T_{\mathrm{eQ}} = 1$. For Boron Nitride we take: $\delta_{\mathrm{r0}} = 0.4$, $E_{\mathrm{r}} = 20$ eV and $E_1 = 50$ eV.

The electron local net energy flux deposited at the wall is

$$P''_{\mathrm{neW}} = -\frac{j_{\mathrm{ne}}}{e}\mathcal{E}_{\mathrm{eW}}, \quad \mathcal{E}_{\mathrm{eW}} = \frac{2T_{\mathrm{eQ}} - 2T_{\mathrm{s}}\delta_{\mathrm{s}}}{1-\delta_{\mathrm{s}}}, \tag{32}$$

where $\mathcal{E}_{\mathrm{eW}}$ is the average energy per net wall-collected electron, and $2T_{\mathrm{s}}$ is the average energy per wall-emitted electron, which is set to 0.4 eV in the simulations here.

At the quasineutral sheath edge Q (i.e., boundary of the simulation domain) the net electron energy flux is

$$P''_{\mathrm{neQ}} = P''_{\mathrm{neW}} - j_{\mathrm{ne}}\phi_{\mathrm{WQ}}. \tag{33}$$

The kinetic electron model inside the sheath is matched with the fluid electron model of the outer quasineutral domain. Current conservation in the sheath imposes j_{ne} in Eq. (29) be equal to that given by the Ohm's law in Eq. (3). The energy flux from the sheath model P''_{neQ} in Eq. (33), is set equal to that from the quasineutral domain, $\mathbf{1}_{\mathrm{n}} \cdot \boldsymbol{P}''_{\mathrm{e}} = -5T_{\mathrm{eQ}} j_{\mathrm{ne}}/(2e) + q_{\mathrm{ne}}$, with $\boldsymbol{P}''_{\mathrm{e}}$ from Eq. (12), thus providing the boundary condition for the electron fluid model. This yields the heat flux at Q as

$$q_{\mathrm{ne}} = -\frac{j_{\mathrm{ne}}}{e}\left(e\phi_{\mathrm{WQ}} + \mathcal{E}_{\mathrm{eW}} - \frac{5}{2}T_{\mathrm{eQ}}\right). \tag{34}$$

For ions, the PIC solution in the quasineutral domain is also matched to the kinetic sheath model at the sheath edge. Dedicated particle-to-surface weighting schemes for the PIC formulation of ions [19, 62, 63] yield directly the net ion power density at Q, P''_{niQ}. Then, the power density deposited at the wall is $P''_{\mathrm{niW}} = P''_{\mathrm{niQ}} + j_{\mathrm{ni}}\phi_{\mathrm{WQ}}$ and the average energy per wall-impacting ion is

$$\mathcal{E}_{\mathrm{iW}} = \frac{eP''_{\mathrm{niW}}}{j_{\mathrm{ni}}}. \tag{35}$$

Acknowledgments

We thank PhD candidate Jesús Perales-Díaz for his active collaboration in the development of the numerical models and constructive comments. This work has been supported by the CHEOPS LOW POWER project, funded by the European Union's Horizon 2020 Research and Innovation Program, under Grant Agreement number 101004331.

References

[1] Kim, V., "Main physical features and processes determining the performance of stationary plasma thrusters," *J. Propulsion Power*, Vol. 14, No. 5, 1998, pp. 736–743.

[2] Zhurin, V., Kaufman, H., and Robinson, R., "Physics of closed drift thrusters," *Plasma Sources Sci. Technol.*, Vol. 8, 1999, p. 1.

[3] Sercel, J., "An experimental and theoretical study of the ECR plasma engine," Ph.D. thesis, California Institute of Technology, 1993.

[4] Packan, D., Elias, P., Jarrige, J., Merino, M., Sánchez-Villar, A., Ahedo, E., Peyresoubes, G., Holste, K., Klar, P., Bekemans, M., Scalais, T., Bourguignon, E., Zurbach, S., Mares, M., Hooque, A., and Favier, P., "The MINOTOR H2020 project for ECR thruster development," 35^{th} *International Electric Propulsion Conference*, Electric Rocket Propulsion Society, 2017.

[5] Takahashi, K., Charles, C., Boswell, R., and Ando, A., "Performance improvement of a permanent magnet helicon plasma thruster," *Journal of Physics D: Applied Physics*, Vol. 46, No. 35, 2013, p. 352001.

[6] Shinohara, S., Nishida, H., Tanikawa, T., Hada, T., Funaki, I., and Shamrai, K. P., "Development of electrodeless plasma thrusters with high-density helicon plasma sources," *IEEE Transactions on Plasma Science*, Vol. 42, No. 5, 2014, pp. 1245–1254.

[7] Toson, E., Moretto, D., Magarotto, M., and et al., "Development and Testing of a Miniature Helicon Plasma Thruster," *35th International Electric Propulsion Conference, Atlanta, GA, IEPC-2017-519*, 2017.

[8] Navarro-Cavallé, J., Wijnen, M., Fajardo, P., and Ahedo, E., "Experimental characterization of a 1 kW helicon plasma thruster," *Vacuum*, Vol. 149, 2018, pp. 69–73.

[9] Parra, F., Ahedo, E., Fife, M., and Martínez-Sánchez, M., "A two-dimensional hybrid model of the Hall thruster discharge," *Journal of Applied Physics*, Vol. 100, 2006, p. 023304.

[10] Garrigues, L., Santhosh, S., Grimaud, L., and Mazouffre, S., "Operation of a low-power Hall thruster: comparison between magnetically unshielded and shielded configuration," *Plasma Sources Science and Technology*, Vol. 28, No. 3, 2019.

[11] Mikellides, I., and Katz, I., "Numerical simulations of Hall-effect plasma accelerators on a magnetic-field-aligned mesh," *Physical Review E*, Vol. 86, No. 4, 2012, p. 046703.

[12] Magarotto, M., Melazzi, D., and Pavarin, D., "3D-VIRTUS: Equilibrium condition solver of radio-frequency magnetized plasma discharges for space applications," *Computer Physics Communications*, Vol. 247, 2020, p. 106953.

[13] Zhou, J., Pérez-Grande, D., Fajardo, P., and Ahedo, E., "Numerical treatment of a magnetized electron fluid within an electromagnetic plasma thruster code," *Plasma Sources Science and Technology*, Vol. 28, No. 11, 2019, p. 115004.

[14] Zhou, A., J. Domínguez-Vazquez, Fajardo, P., and Ahedo, E., "Magnetized fluid electron model within a two-dimensional hybrid simulation code for electrodeless plasma thrusters," *Plasma Sources Science and Technology*, accepted for publication.

[15] Marks, T. A., Mikellides, I. G., Lopez Ortega, A., and Jorns, B., "Hall2De Simulations of a Magnetic Nozzle," *AIAA Propulsion and Energy 2020 Forum*, 2020.

[16] Ahedo, E., Correyero, S., Navarro, J., and Merino, M., "Macroscopic and parametric study of a kinetic plasma expansion in a paraxial magnetic nozzle," *Plasma Sources Science and Technology*, Vol. 29, No. 4, 2020, p. 045017. https://doi.org/10.1088/1361-6595/ab7855.

[17] Merino, M., Mauriño, J., and Ahedo, E., "Kinetic electron model for plasma thruster plumes," *Plasma Sources Science and Technology*, Vol. 27, No. 3, 2018, p. 035013. https://doi.org/10.1088/1361-6595/aab3a1.

[18] Li, M., Merino, M., Ahedo, E., and Tang, H., "On electron boundary conditions in PIC plasma thruster plume simulations," *Plasma Sources Science and Technology*, Vol. 28, No. 03, 2019, p. 034004. https://doi.org/10.1088/1361-6595/ab0949.

[19] Domínguez-Vázquez, A., "Axisymmetric simulation codes for Hall effect thrusters and plasma plumes," Ph.D. thesis, Universidad Carlos III de Madrid, Leganés, Spain, 2019.

[20] Domínguez-Vázquez, A., Zhou, J., Fajardo, P., and Ahedo, E., "Analysis of the plasma discharge in a Hall thruster via a hybrid 2D code," 36^{th} *International Electric Propulsion Conference*, Electric Rocket Propulsion Society, Vienna, Austria, 2019.

[21] Perales-Díaz, J., Domínguez-Vázquez, A., Fajardo, P., Ahedo, E., Faraji, F., Reza, M., and Andreussi, T., "Hybrid plasma simulations of the HT5k thruster," *ExB Plasmas Workshop, Young researchers "poster" mini-session*, Madrid, Spain, February 16-18, 2022.

[22] Perales-Díaz, J., Domínguez-Vázquez, A., Fajardo, P., Ahedo, E., Faraji, F., Reza, M., and Andreussi, T., "Hybrid plasma simulations of a magnetically shielded Hall thruster," *Journal of Applied Physics*, Vol. 131, No. 10, 2022. https://doi.org/10.1063/5.0065220.

[23] Zhou, J., "Modeling and simulation of the plasma discharge in a radiofrequency thruster," Ph.D. thesis, Universidad Carlos III de Madrid, Leganés, Spain, 2021.

[24] Domínguez-Vázquez, A., Cichocki, F., Merino, M., Fajardo, P., and Ahedo, E., "Axisymmetric plasma plume characterization with 2D and 3D particle codes," *Plasma Sources Science and Technology*, Vol. 27, No. 10, 2018, p. 104009. https://doi.org/10.1088/1361-6595/aae702.

[25] Domínguez-Vázquez, A., Cichocki, F., Merino, M., Fajardo, P., and Ahedo, E., "On heavy particle-wall interaction in axisymmetric plasma discharges," *Plasma Sources Science and Technology*, Vol. 30, No. 8, 2021, p. 085004. https://doi.org/10.1088/1361-6595/ac1715, URL https://doi.org/10.1088/1361-6595/ac1715.

[26] Pérez-Grande, D., "Fluid modeling and simulation of the electron population in Hall effect thrusters with complex magnetic topologies," Ph.D. thesis, Universidad Carlos III de Madrid, Leganés, Spain, 2018.

[27] Pérez-Grande, D., González-Martínez, O., Fajardo, P., and Ahedo, E., "Analysis of the numerical diffusion in anisotropic mediums: benchmarks for magnetic field aligned meshes in space propulsion simulations," *Applied Sciences*, Vol. 6, No. 11, 2016, p. 354.

[28] Fife, J. M., "Hybrid-PIC modeling and electrostatic probe survey of Hall thrusters," Ph.D. thesis, Massachusetts Institute of Technology, 1998.

[29] Bittencourt, J., *Fundamentals of plasma physics*, Springer, Berlin, Germany, 2004.

[30] Hara, K., "An overview of discharge plasma modeling for Hall effect thrusters," *Plasma Sources Science and Technology*, Vol. 28, No. 4, 2019, p. 044001.

[31] Parra, F. I., Ahedo, E., Fife, J. M., and Martínez-Sánchez, M., "A two-dimensional hybrid model of the Hall thruster discharge," *Journal of Applied Physics*, Vol. 100, No. 2, 2006, p. 023304.

[32] Cichocki, F., Domínguez-Vázquez, A., Merino, M., and Ahedo, E., "Hybrid 3D model for the interaction of plasma thruster plumes with nearby objects," *Plasma Sources Science and Technology*, Vol. 26, No. 12, 2017, p. 125008.

[33] Stephen Francis Biagi, "Cross sections extracted from PROGRAM MAGBOLTZ, VERSION 7.1 JUNE 2004," , June 2004. URL www.lxcat.net/Biagi-v7.1, [Online; accessed 5-July-2021].

[34] Mitchner, M., and Kruger Jr., C., *Partially ionized gases*, John Wiley and Sons, Hoboken, NJ, 1973.

[35] Boeuf, J., and Garrigues, L., "Low frequency oscillations in a stationary plasma thruster," *J. Applied Physics*, Vol. 84, No. 7, 1998, pp. 3541–3554.

[36] Ahedo, E., Gallardo, J., and Martínez-Sánchez, M., "Effects of the radial-plasma wall interaction on the axial Hall thruster discharge," *Physics of Plasmas*, Vol. 10, No. 8, 2003, pp. 3397–3409.

[37] Petra, C. G., Schenk, O., Lubin, M., and Gärtner, K., "An augmented incomplete factorization approach for computing the Schur complement in stochastic optimization," *SIAM Journal on Scientific Computing*, Vol. 36(2), 2014, pp. C139–C162.

[38] Petra, C. G., Schenk, O., and Anitescu, M., "Real-time stochastic optimization of complex energy systems on high-performance computers," *Computing in Science and Engineering*, Vol. 16(5), 2014, pp. 32–34.

[39] Meeker, D., *FEMM User's Manual Version 4.2*, 2020.

[40] Mikellides, I., Katz, I., Goebel, D. M., Jameson, K. K., and Polk, J. E., "Wear mechanisms in electron sources for ion propulsion, 2: Discharge hollow cathode," *Journal of Propulsion and Power*, Vol. 24, No. 4, 2008, pp. 866–879.

[41] Mazouffre, S., Echegut, P., and Dudeck, M., "A calibrated infrared imaging study on the steady state thermal behaviour of Hall effect thrusters," *Plasma Sources Science and Technology*, Vol. 16, No. 1, 2006, p. 13.

[42] Moore, P., and Sowter, A., "Application of a satellite aerodynamics model based on normal and tangential momentum accommodation coefficients," *Planetary and space science*, Vol. 39, No. 10, 1991, pp. 1405–1419.

[43] Moe, K., and Moe, M., "Gas–surface interactions and satellite drag coefficients," *Planetary and Space Science*, Vol. 53, No. 8, 2005, pp. 793–801.

[44] Miller, J., Pullins, S., Levandier, D., Chiu, Y., and Dressler, R., "Xenon charge exchange cross sections for electrostatic thruster models," *Journal of Applied Physics*, Vol. 91, No. 3, 2002, pp. 984–991.

[45] Hagelaar, G., Bareilles, J., Garrigues, L., and Boeuf, J., "Role of anomalous electron transport in a stationary plasma thruster simulation," *Journal of Applied Physics*, Vol. 93, No. 1, 2003, pp. 67–75.

[46] Koo, J., and Boyd, I., "Modeling of anomalous electron mobility in Hall thrusters," *Physics of Plasmas*, Vol. 13, 2006, p. 033501.

[47] Santos, R., "Código híbrido avanzado de motores de plasma de efecto Hall," Ph.D. thesis, Universidad Politécnica de Madrid (UPM), Madrid, Spain, 2012.

[48] Bareilles, J., Hagelaar, G., Garrigues, L., Boniface, C., Boeuf, J., and Gascon, N., "Critical assessment of a two-dimensional hybrid Hall thruster model: Comparisons with experiments," *Physics of Plasmas*, Vol. 11, No. 6, 2004, pp. 3035–3046.

[49] Fife, J., Martínez-Sánchez, M., and Szabo, J., "A Numerical Study of Low-Frequency Discharge Oscillations in Hall Thrusters," *33rd Joint Propulsion Conference, Seattle, WA*, 1997.

[50] Choueiri, E., "Plasma oscillations in Hall thrusters," *Physics of Plasmas*, Vol. 8, No. 4, 2001, pp. 1411–1426.

[51] Barral, S., and Ahedo, E., "Low-frequency model of breathing oscillations in Hall discharges," *Physical Review E*, Vol. 79, 2009, p. 046401.

[52] Jorns, B. A., and Byrne, M. P., "Model for the dependence of cathode voltage in a Hall thruster on facility pressure," *Plasma Sources Science and Technology*, Vol. 30, No. 1, 2021, p. 18.

[53] Goebel, D., and Katz, I., *Fundamentals of Electric Propulsion: Ion and Hall Thrusters*, Jet Propulsion Laboratory, Pasadena, CA, 2008.

[54] Ahedo, E., and Pablo, V. d., "Combined effects of electron partial thermalization and secondary emission in Hall thruster discharges," *Physics of Plasmas*, Vol. 14, 2007, p. 083501.

[55] Domínguez-Vázquez, A., Taccogna, F., and Ahedo, E., "Particle modeling of radial electron dynamics in a controlled discharge of a Hall thruster," *Plasma Sources Science and Technology*, Vol. 27, No. 6, 2018, p. 064006.

[56] Domínguez-Vázquez, A., Taccogna, F., Fajardo, P., and Ahedo, E., "Parametric study of the radial plasma-wall interaction in a Hall thruster," *Journal of Physics D: Applied Physics*, Vol. 52, No. 47, 2019, p. 474003. https://doi.org/10.1088/1361-6463/ab3c7b, URL https://doi.org/10.1088%2F1361-6463%2Fab3c7b.

[57] Marín-Cebrián, A., Domínguez-Vázquez, A., Fajardo, P., and Ahedo, E., "Macroscopic plasma analysis from 1D-radial kinetic results of a Hall thruster discharge," *Plasma Sources Science and Technology*, Vol. 30, No. 11, 2021, p. 115011. https://doi.org/10.1088/1361-6595/ac325e, URL https://doi.org/10.1088/1361-6595/ac325e.

[58] Hobbs, G., and Wesson, J., "Heat flow through a Langmuir sheath in the presence of electron emission," *Plasma Physics*, Vol. 9, 1967, p. 85.

[59] Ahedo, E., "Presheath/sheath model of a plasma with secondary emission from two parallel walls," *Physics of Plasmas*, Vol. 9, No. 10, 2002, pp. 4340–4347.

[60] Barral, S., Makowski, K., Peradzynski, Z., Gascon, N., and Dudeck, M., "Wall material effects in stationary plasma thrusters. II. Near-wall and in-wall conductivity," *Phys. Plasmas*, Vol. 10, No. 10, 2003, pp. 4137–4152.

[61] Taccogna, F., Longo, S., and Capitelli, M., "Plasma sheaths in Hall discharge," *Physics of Plasmas*, Vol. 12, No. 9, 2005, p. 093506.

[62] Santos, R., and Ahedo, E., "Implementation of the Kinetic Bohm Condition in a Hall Thruster Hybrid Code," *45th Joint Propulsion Conference*, AIAA, Reston, VA, Denver, Colorado, August 2-5, 2009.

[63] Ahedo, E., Santos, R., and Parra, F., "Fulfillment of the kinetic Bohm criterion in a quasineutral particle-in-cell model," *Physics of Plasmas*, Vol. 17, No. 7, 2010, p. 073507.